Recent advances on applications of NV⁻ magnetometry in condensed matter physics

Ying Xu,[†] Weiye Zhang,[†] and Chuanshan Tian* [ID]

Department of Physics, Fudan University, Shanghai 200438, China
Corresponding author: cstian@fudan.edu.cn

Measuring magnetic response from spin and current is of fundamental interest in condensed matter physics. Negatively charged nitrogen-vacancy (NV⁻) centers in diamond are emerging as a robust and versatile quantum sensor owing to their high sensitivity, nanometer-scale spatial resolution, and noninvasive operation with access to static and dynamic magnetic and electron transport properties. In this review, we discuss the rapidly growing interest in the implementation of NV⁻ magnetometry to explore condensed matter physics, focusing on three topics: anti/ferromagnetic materials, superconductors, and metals/semimetals/semiconductors. © 2023 Chinese Laser Press

https://doi.org/10.1364/PRJ.471266

1. INTRODUCTION

Many new materials displaying exciting physical phenomena have been discovered and explored in the past decades. Examples include novel superconductors (SCs) [1–3], van der Waals materials [4,5], topological insulators [6,7], and multiferroic materials [8,9]. The emergence of these new systems challenges traditional measurement schemes in characterizing their magnetic properties in terms of sensitivity, spatial resolution, dynamic range, etc. Generally, the characterization of condensed matter materials with magnetometry [10,11] mainly focuses on probing four types of magnetic fields generated by spins and currents [11]: (1) static spin configuration of a magnetic system, such as domain wall (DW) and skyrmion; (2) dynamic field produced by the excitations of magnetic systems, e.g., spin-wave; (3) field generated by static current distributions; and (4) field noise created by current fluctuations. Various magnetic measurement schemes have been proposed for different needs. Spin-resolved magnetometric techniques, such as muon spectroscopy [12], nuclear magnetic resonance (NMR) [13,14], and neutron scattering [15], enable noninvasive wide-field measurement of the magnetic structure of a material. On the other hand, scanning probe-based approaches, such as magnetic force microscopy (MFM) [16,17] and scanning superconducting quantum interference devices (scanning SQUIDs) [10,18], allow real-space imaging of the magnetic fields emanating from nanoscale samples. However, the spin-resolved techniques offer a poor spatial resolution that cannot resolve nanoscale magnetic structure, while the scanning techniques either act as perturbative probes or can only work over a narrow temperature range. The electronic spin of the negatively charged nitrogen-vacancy (NV⁻) center in diamond

is emerging as a robust and versatile quantum sensor for non-invasive detection of weak magnetic fields [19]. Since the pioneering works [20–22], NV⁻ magnetometry has demonstrated its unique advantages in comparison to other magnetic-sensing techniques: single-electron and individual-proton sensitivity [23,24], nanometer-scale spatial resolution [25], and high tolerance of working temperature [26–28] (from ∼1 K to above room temperature) and pressure [29–32] (from ultra-high vacuum to >60 GPa).

In this review, we outline some recent advances in NV⁻ magnetometry and its applications in the study of magnetic and transport properties in condensed matter systems. We begin with a summary of the NV⁻ properties and experimental techniques. Next, we discuss the implementation of NV⁻ magnetometry to study magnetic phenomena in condensed matter materials with emphasis on anti/ferrimagnetism, SC, and metal/semimetal/semiconductors. In the case of antiferrimagnetic/ferrimagnetic materials, the high spatial resolution of the NV⁻ magnetometry was used to determine the nature of antiferromagnetic/ferromagnetic (AFM/FM) spin textures. Meanwhile, the high spectral resolution of NV⁻ magnetometry was employed in the study of spin-waves in FM materials. In the following section, we discuss the application of NV⁻ magnetometry in SCs. Owing to its merit of operation under a broad range of temperatures and pressures, NV⁻ magnetometry is a unique tool to determine the transition temperature and the critical field, and to map the spatial structure of magnetic responses in various superconducting materials. Finally, we focus on the dc and dynamic magnetic field created by current flow or fluctuations in metal/semimetal/semiconductor nanostructures and thin films. In this aspect, the noninvasive

NV$^-$ magnetometry with high-spatial resolution finds its unique advantage in mapping distribution of the local current density and its fluctuation.

2. PRINCIPLES OF NV$^-$ MAGNETOMETRY

The properties and measurement schemes of NV$^-$ centers have been summarized in some well-noted review papers [11,19,33–36]. Here we briefly outline the fundamental properties and some basic NV$^-$ center measurement schemes to clarify nomenclatures in the following discussion. The NV$^-$ center is a type of point defect in the diamond lattice [Fig. 1(a)] with its energy-level structure shown in Fig. 1(b). At present, most of the experiments on NV$^-$ centers are carried out via manipulation and detection of electron spins in the ground state (GS) $^3A_2$. The electron spins are first initialized to $m_s = 0$ through off-resonant optical excitation. Then, the spins are actively controlled by resonant microwave pulses, and the environmental magnetic information is encoded into the spin states. Finally, the population of electrons in different spin states is read out by fluorescence difference because the photoluminescence efficiency of electrons in $m_s = \pm 1$ states is 30% lower than that of electrons in $m_s = 0$ state [33,34]. The sensing ability of NV$^-$ centers to the magnetic field comes from the Zeeman splitting $2h\gamma B$ between $m_s = \pm 1$ states when external magnetic field B is applied along the NV axis, where $\gamma = 2.8$ MHz/G is the gyromagnetic ratio and h is the Planck constant.

In applying NV$^-$ magnetometry to condensed matter materials, detection sensitivity and spatial resolution are two primary factors to be considered. In the following, we discuss the sensitivity and spatial resolution of NV$^-$ magnetometry and introduce some techniques aiming at optimizing sensitivity and enhancing spatial resolution.

A. Sensitivity of NV Magnetometry

By adopting different magnetic-sensing protocols, the NV$^-$ center can be used to measure both dc and ac magnetic responses. The sensitivity of NV$^-$ dc and ac magnetometry is generalized with one equation,

$$\eta = \alpha \underbrace{\frac{1}{2\pi\gamma} \frac{1}{\sqrt{N\tau}}}_{\text{spin projection limit}} \underbrace{\frac{1}{e^{-(\tau/T)^p}}}_{\text{spin dephasing}} \underbrace{\sqrt{1 + \frac{1}{C^2 n_{\text{avg}}}}}_{\text{readout}} \underbrace{\sqrt{\frac{t_I + \tau + t_R}{\tau}}}_{\text{overhead time}},$$

(1)

which consists of four contributions: spin projection limit, spin dephasing, readout, and overhead time [36]. The spin-projection-limited sensitivity was pointed out by Taylor *et al.* [22], where $\gamma = 2.8$ MHz/G is the electron gyromagnetic ratio, N is the number of NV$^-$ centers in the ensemble, τ is the free-precession (i.e., interrogation) time per measurement, $T = T_2^*$ for dc magnetometry limited by the inhomogeneous dephasing time T_2^*, and $T = T_2$ for ac magnetometry limited by the coherence time T_2. The constant α represents the difference of the effective field value between dc and ac signal, with $\alpha = 1$ for dc Ramsey magnetometry, and $\alpha = \pi/2$ for ideal ac Hahn echo magnetometry [36]. Some pulsed magnetometry schemes such as Ramsey-based protocols can achieve sensitivities approaching the spin projection limit [22,37]. However, they still suffer from spin dephasing and experimental nonidealities including imperfect readout and overhead time, which deteriorate the achievable sensitivity [22,38].

First, the sensitivity η is degraded for increased values of τ due to spin dephasing during precession. For instance, in dc Ramsey-type magnetometry, the dephasing occurs with inhomogeneous dephasing time T_2^* so that η is deteriorated by the following factor:

$$\frac{1}{e^{-(\tau/T)^p}}.$$

(2)

Here $T = T_2^*$, and the stretched exponential parameter p is related to the spin bath surrounding the NV center [39–41].

Second, the conventional NV$^-$ optical readout technique does not allow single-shot determination of the NV$^-$ spin state, further degrading the sensitivity due to the spin projection limit as accounted for by the readout factor in Eq. (1). Following the work of Shields *et al.* [38], the readout factor is denoted by $\sigma_R \geq 1$, and $\sigma_R = 1$ corresponds to readout at the spin
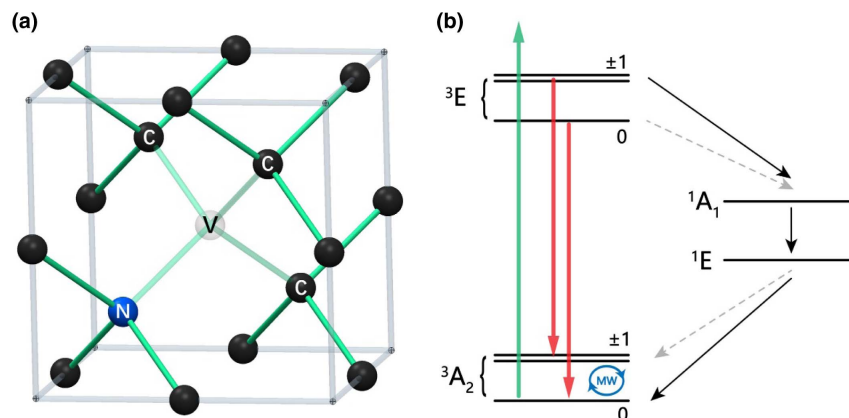

Fig. 1. Properties of the nitrogen-vacancy center. (a) Illustration of the nitrogen-vacancy center and diamond lattice. Transparent, the vacancy; blue, the substitutional nitrogen atom; black, carbon atoms. (b) Relevant electronic energy levels of NV$^-$. The NV$^-$ center is excited by 532 nm laser pulses off-resonantly (green arrow), and fluorescent photons from ~600 to ~800 nm are collected (red arrow). The strong (weak) intersystem crossings between spin-triplet states and spin-singlet states ($^3E \rightarrow {}^1A_1$, $^1E \rightarrow {}^3A_2$) are denoted by solid black (dashed gray) arrows. The spin states in the ground state ($^3A_2$) can be manipulated by microwave (MW) excitation.

projection limit. This parameter is the inverse of the measurement fidelity $\mathcal{F} = 1/\sigma_R$. For imperfect readout, the value of σ_R can be calculated as

$$\sigma_R = \sqrt{1 + \frac{1}{C^2 \eta_{\mathrm{avg}}}} = \sqrt{1 + \frac{2(a_0 + a_1)}{(a_0 - a_1)^2}}, \qquad (3)$$

where a_0 and a_1, respectively, denote the average numbers of photons detected when the NV$^-$ is projected into $m_s = 0$ or $m_s = \pm 1$ states per readout. Following Barry *et al.*'s discussion [36], $C = (a_0 + a_1)/(a_0 - a_1)$ is identified as the measurement contrast, and $\eta_{\mathrm{avg}} = (a_0 + a_1)/2$ is the average number of photons collected per NV$^-$ center per measurement.

Third, when certain readout techniques, such as spin-to-charge conversion (SCC) or super-resolution microscopy (SRM) techniques, are applied, the spin state initialization time t_I and readout time t_R can be significant compared to the interrogation time τ. This nonideality can be quantified by the fraction of time devoted to spin precession:

$$\sqrt{\frac{t_I + \tau + t_R}{\tau}}. \qquad (4)$$

1. Improving Sensitivity

Currently, methods to enhance sensitivity can be divided into two categories: (1) extending the coherence time and (2) improving the readout fidelity.

Coherence time extension. The sensitivity of dc NV$^-$ magnetometry is primarily limited by the inhomogeneous dephasing time T_2^*, which can only be slightly extended by spin bath driving [42–44], transverse strain, and electric-field mitigation [45,46]. In comparison, the ac signal detection in the range of 10 kHz–10 MHz could take full advantage of Hahn echo or dynamical decoupling (DD) techniques that have been widely adopted in NMR [37,47], where superposition of the spin states is first prepared followed by a series of synchronized control pulses. The magnetic field can then be deduced from the accumulated phase during the spin manipulation processes. These ac protocols significantly reduce the dephasing and enhance the sensitivity to approach the intrinsic limitation set by the coherence time T_2 (Hahn echo) and $T_2^{(k)} = k^s T_2$ (DD), where k is the number of pulses and s is related to the noise spectrum of the decohering spin bath and is typically sublinear [22,36,48,49]. Magnetometry is also feasible in the MW frequency range (100 MHz–10 GHz) by measuring the Rabi oscillation (hereto denoted as the MW Rabi method) between the spin states [50–52]. Its sensitivity is generally limited by T_2^*, but through the implementation of the DD technique, it can be improved to T_2-limited boundary as demonstrated in recent works [53,54].

Readout fidelity enhancement. The readout fidelity of NV$^-$ spin can benefit from optical methodologies. A seminal example is the SCC readout. Unlike the conventional readout approach, in SCC, the spin state of NV$^-$ is mapped onto the charge state of the NV color defect, NV^0 and NV$^-$, which can be detected more accurately by measuring the fluorescence differences at the optimal excitation wavelength. This technique can be applied to both single NV [38,55–57] and ensembles either in nanodiamonds [58] or bulk diamonds
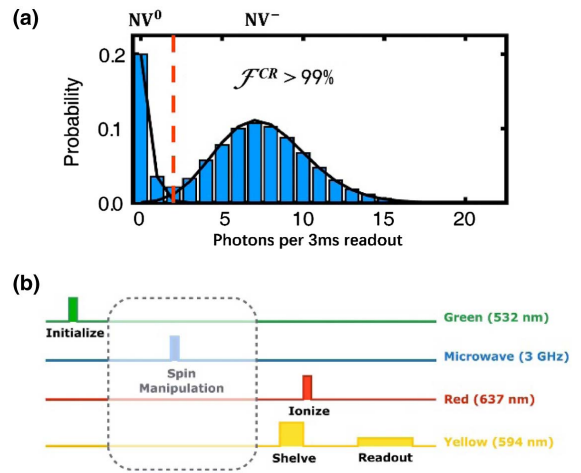

Fig. 2. Principle of spin to charge conversion readout. (a) High fidelity charge-state determination of NVs. During each readout, NV$^-$ statically emits far more photons than NV^0 as shown by the blue histogram. The charge-state determination of NVs is realized by setting a threshold indicated by the red dashed line. The photon readout rate from NV^0 becomes negligible above the threshold. Adapted from Ref. [55]. (b) Schematic of the spin-to-charge conversion readout protocol used in Ref. [38]. Adapted from Ref. [57].

[59]. The key advantage of SCC readout over conventional spin-state-dependent fluorescence readout is that, unlike the spin state, the charge state is stable under 594 nm excitation and NV$^-$ is much brighter than NV^0; hence, by repeated excitation, the photon difference provides a sharp contrast to allow single-shot determination of the charge state. Under 594 nm excitation, NV$^-$ is ~40 times brighter than NV^0, as the excitation wavelength is shorter than the zero-phonon line (ZPL) of NV$^-$ (637 nm) but longer than the ZPL of NV^0 (575 nm). In Fig. 2(a), a clear difference can be seen in the photon emission rate between NV^0 and NV$^-$ at an unsaturated excitation power, and charge-state determination with fidelity $\mathcal{F}^{\mathrm{CR}} > 99\%$ has been demonstrated by setting a photon detection threshold [55]. With the reliable charge state readout, the next step is to map the NVs' spin states onto the charge states. In the protocol proposed by Shields *et al.* [38], a green ~532 nm light is used to transfer the single NV center preferentially to NV$^-$ with 70%–75% probability [60] and to prepare the NV in the $m_s = 0$ spin state. Next, with appropriate MWs, the NV$^-$ is further prepared in a superposition of the $m_s = 0$ or one of the $m_s = \pm 1$ states. After that, a ~50 ns 594 nm yellow "shelving" pulse with moderate power (145 μW, ~90 mW/cm^2) excites the spin population to the triplet excited state (ES). Due to the spin-dependent intersystem crossing rate from the triplet ES, the $m_s = \pm 1$ population is more likely to be shelved into the metastable singlet states, whereas $m_s = 0$ population just decays back to the original state. The SCC is then realized with a ~10 ns high-intensity resonant 637 nm pulse (22.5 mW, ~14 W/cm^2) immediately applied after the "shelving" pulse, which selectively ionizes (i.e., converts NV$^-$ to NV^0) the triplet GS population (corresponding to $m_s = 0$) via absorption of two photons, while leaving the shelved metastable singlet population

(corresponding to $m_s = \pm 1$) unaffected. To this end, the spin state is successfully mapped onto the charge state of the color center. Finally, the NV charge state is read out by applying weak 594 nm light (~ 1–$10~\mu W$, ~ 0.6–$6~mW/cm^2$), as shown in Fig. 2(b). The total fidelity of SCC can reach $\mathcal{F} = \mathcal{F}^{CR} \times \mathcal{F}^{SCC} = 0.36$, where the dominant limitation is set by the SCC efficiency ($\mathcal{F}^{SCC} = 0.37$). Other SCC variants exploiting ionization of the singlet state [55] or with reduced experimental complexity [58] have also demonstrated similar sensitivity. However, all SCC schemes require significantly prolonged readout time t_R, which is on the order of several hundreds of micro-seconds [38,58]. This would reduce the sensitivity enhancement when t is smaller than t_R. Hence, SCC is most suitable in NV^- magnetometry with a long sensing period, such as relaxometry and ac magnetic field sensing.

Another approach to improve readout fidelity is increasing the photon collection efficiency η. In the limit of low contrast, the readout fidelity $\mathcal{F}$ is proportional to the square root of η_{avg}. Conventionally, an objective with a large numerical aperture (NA) is used to collect photons emitted from NVs in a bulk diamond. The photon collection efficiency η_{avg} is mainly hindered by the total reflection at the flat diamond interface. The effective NA of the objective is degraded by a factor equal to the refractive index of diamond ($n_d = 2.4$), resulting in a photon detection rate <3% for a 0.8 NA objective [61].

2. Enhancing Photon Collection Efficiency

Proper optical techniques such as side collection [62] and parabolic concentrators [63,64] allow much higher photon collection efficiency. For the NV^- ensemble, one approach is to collect the photons exiting from the side of the diamond. According to the calculation of Le Sage *et al.* [61], $\approx 91\%$ of photons are confined by the total internal reflection between the polished top and bottom surfaces of the diamond chip. On the other hand, $\approx 29\%$ of photons could reach the four

sides of the diamond chip on the first incidence at the edges of the diamond chip. Hence, a photon collection efficiency of $29\% < \eta < 91\%$ for the side-collection technique can be expected. Experimentally, they demonstrated a collection efficiency of 39% by detecting photons exiting from the four sides of the diamond chip via four photodiodes deposited at the edges. Following the same approach, Ma *et al.* designed a simpler device that used coupling prisms to direct light exiting from the diamond's four side faces to the detector and demonstrated a collection efficiency of 40% [62], as shown in Fig. 3(a). Figure 3(b) presents another approach using parabolic concentrators. In 2015, Wolf *et al.* employed a parabolic-shaped glass lens contacting with the top side of the diamond to improve collection efficiency [63]. The critical angle at the glass/diamond interface would be larger due to the higher refractive index of glass compared to that of air. Thus, it enhances the output coupling efficiency. The collected light is then collimated by the parabolic surface of the glass lens and directed to the detector. According to their simulation, the collection efficiency is about 65%. However, they did not perform a dedicated experiment to confirm this result. Furthermore, the two methods mentioned above can be combined, and the collection efficiency in bulk NV-diamond magnetometers may be improved to near 100%, limited only by losses due to absorption [36]. For example, one can first redirect the light to the bottom side of the diamond with dielectric or metallic reflectors [66] and use a parabolic concentrator to collect the light with high efficiency.

In the case of single NV, for bulk diamond, a common approach to minimizing oblique reflections at the diamond–air interface is to fabricate a hemispherical surface, known as a solid immersion lens (SIL), close to the NV center of interest [67–70]. In the experiment by Zhang *et al.*, a photon detection rate of approximately 1 Mcps (cps, counts per second) with 0.9 NA objective was demonstrated [70]. An alternative approach
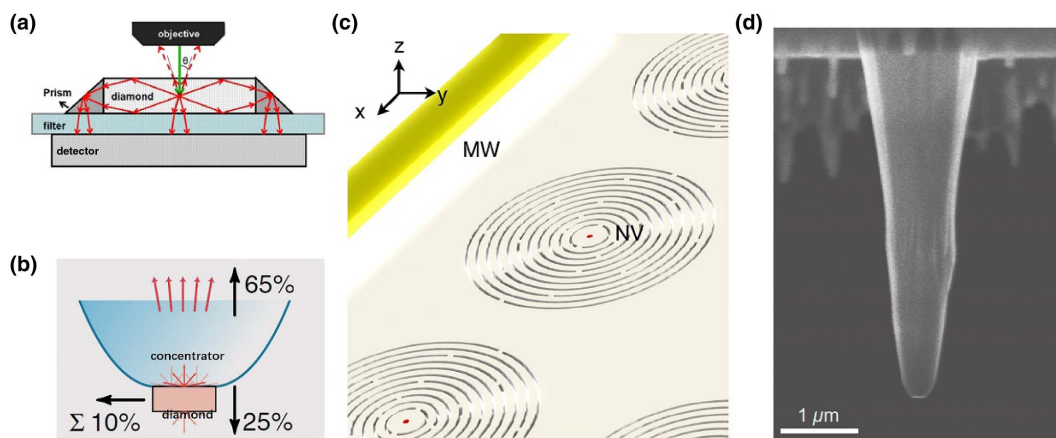

Fig. 3. Methods to improve photon collection rate. (a) Schematic of high efficiency side collection with coupling prisms on four sides of the diamond. Reprinted with permission from Ref. [55]. Copyright 2016 American Physical Society. (b) Schematic of the parabolic collector. 65% of the photons emitted from the NVs are coupled to the concentrator according to simulation. Adapted from Ref. [63]. (c) Illustration of an array of diamond circular bullseye gratings adjacent to a microwave (MW) strip line. Reprinted with permission from Ref. [65]. Copyright 2015 American Chemical Society. (d) SEM image of the nanopillar, consisting of parabolic tip and tapered waveguide. Reprinted with permission from Ref. [64]. Copyright 2020 American Physical Society.

is to attach a dielectric SIL with a refractive index even higher than diamond to the diamond surface. So far, gallium phosphide (GaP), with an index of 3.3, is the available SIL material showing a higher index than diamond and transparency over the NV emission spectrum [71,72]. Experimentally, Riedel _et al._ achieved a photon detection rate of 0.6 Mcps with 0.8 NA objective and a hemispherical GaP SIL [72]. Besides fabricating SILs, carving concentric slits whose period satisfies the second-order Bragg condition, known as bullseye grating [Fig. 3(c)], can also significantly improve photon collection efficiency. With the bullseye grating design, at each slit light scatters with equal phase, leading to constructive interference in the vertical direction. A photon detection rate as high as 4.56 Mcps with 1.3 NA objective was demonstrated [65]. These approaches are suitable for NV$^-$ deeply embedded in the diamond (depth > 100 nm) and are mainly targeted to quantum information as well as quantum computation.

For scanning probe applications, the improvement of photon collection is mainly due to the progress of the nanofabrication. The development of scanning probe fabrication can be divided into three phases. At first, cylindrical nanopillars were fabricated through reactive ion etching (RIE) on masks defined by electron beam lithography (EBL) [73,74]. The photon detection rate of cylindrical nanopillars is ~0.2 Mcps with 0.7 NA objective. Later, Zhou _et al._ demonstrated a simple procedure to create diamond probes for scanning probe applications [75]. In their procedure, minimum fabrication steps are implemented. With an optimized recipe, the fabricated nanopillars hold a slightly tapered shape working as a multimode waveguide, and thus offer better performance (0.2–0.5 Mcps photon detection rate) than cylindrical nanopillars. They also demonstrated the integration of a micro-antenna onto the AFM chip, which delivers RF excitation to the NV center located inside a nanophotonic waveguide structure. This enabled easy implementation of diamond probes to conventional AFM design. More recently, Hedrich _et al._ realized an adapted parabolic geometry suitable for magnetometry by developing a scalable fabrication procedure based on EBL and plasma-etching methods [64]. In their recipe, the key point is that, in the etching process, one will develop the tapered diamond waveguide using O_2-based plasma and then the parabolic tip by adding CF_4 in increasing amounts. Raising the concentration of CF_4 etches the mask more quickly, leading to a steeper angle of the diamond wall. A finished device is shown in Fig. 3(d). The parabolic nanopillars offer a ~2.1 Mcps photon detection rate with 0.8 NA objective, meaning nearly an order of improvement over the cylindrical design.

B. Spatial Resolution of NV$^-$ Magnetometry

One of the key advantages of NV$^-$ magnetometry is the high spatial resolution. For example, using the scanning probe NV$^-$ magnetometry, a spatial resolution of ~10 nm has been realized [27,74,76]. However, there is always a compromise between sensitivity and spatial resolution. In general, the better spatial resolution requires a smaller distance between NV$^-$ centers and the under-investigation sample [11,74,77], while it is well known that, near the diamond surface (<10 nm), poor coherence properties, or equivalently, shorter dephasing time T_2^* and T_2, occur [34,78,79]. Another restriction is the total number of NV$^-$ defects involved in the detection. A single NV$^-$ defect provides the best spatial resolution and better coherence, but the photon shot-noise-limited sensitivity would be sacrificed greatly compared with ensemble detection [36,63,80].

With these considerations, we summarize the current spatial resolution and sensitivity available for the study of condensed matter, as shown in Table 1. For μm to sub-μm resolution, a confocal microscope can nicely fit the need using an ensemble of NV$^-$ defects. To achieve better coherent time, the depth of NV$^-$ defects from the diamond surface can be tens of nm or even ~100 nm. In this case, T_2^* can easily reach several μs, or even up to ~10 μs for ^{12}C purified diamond [91,93,94]. The main restriction on sensitivity is the limited photon collected due to the small quantity of NV$^-$ defects within the focal volume. Increasing nitrogen impurity density beyond 1 ppm (parts per million) is not recommended since that would degrade T_2^* considerably [22]. The longitudinal relaxation time T_1 also benefits from the relatively deep NV$^-$ distribution and can reach ~1 s in a cryogenic environment [95,96]. A detailed discussion can be found in previous excellent reviews [11,19,36].

For spatial resolution beyond the optical diffraction limit, the scanning probe scheme was employed either by attaching a nanodiamond on the scanning tip of atomic force microscopy [81,97] or by fabricating a diamond tip containing a single NV$^-$ [26,27,74,76]. In both cases, the distance between the NV$^-$ center and the diamond surface should be around 10 nm or less to achieve a spatial resolution of ~10 nm. The shortcoming of such NV$^-$ is that the coherence properties are poorer than those in the bulk diamond. Some recent scanning probe NV$^-$ magnetometry applications have demonstrated detection sensitivity of the DC magnetic field around ~μT [27,76,81–83].

Besides employing scanning probes, nanometer-scale spatial resolution of NV$^-$ magnetometry can also be achieved through SRM techniques. Conventionally, the SRM techniques fall into two categories, i.e., deterministic SRM and stochastic SRM,

Table 1. Typical Spatial Resolution and Sensitivity of NV$^-$ Magnetometry Available for Condensed Matter Systems Research[a]

Scheme (Resolution)	Atomic Force Microscope (10–100 nm)	Confocal (~500 nm)	Large Ensemble (~mm)
dc magnetometry	3–10 μT/Hz$^{1/2}$ [26,27,76,81–86]	0.03–3 μT/Hz$^{1/2}$ [87–89]	15 pT/Hz$^{1/2}$ [80]
ac magnetometry	50–100 nT/Hz$^{1/2}$ [23,74,90]	4–100 nT/Hz$^{1/2}$ [91,92]	1 pT/Hz$^{1/2}$ [63]

[a]Also listed here is NV$^-$ magnetometry on a large ensemble for comparison. The best record of sensitivity is shown in the table.

depending on the switching mechanism. Deterministic SRM, such as stimulated emission depletion (STED) microscopy [98–101], ground state depletion (GSD) microscopy [102], spin-reversible saturable optical fluorescence transitions (Spin-RESOLFT) [103,104], and charge state depletion (CSD) [105,106], relies on the nonlinear optical response, especially saturation of the fluorescence to the excitation laser. The sub-diffraction image is realized by a doughnut-shaped excitation light with zero intensity at the center generated by a phase plate.

In STED, an NV is first excited from the GS to the ES. Then it is either deexcited via spontaneous emission (600–800 nm wideband) or stimulated emission (775 nm) by applying a STED beam. In the work of Wildanger *et al.* [98], a ~GW/cm² 775 nm red excitation doughnut beam (STED beam) is applied to deplete the spontaneous emission efficiently. It keeps the NVs' stimulated emission rate much faster than the spontaneous emission rate except for the NVs at the central region. Thus, only the NVs at the central region contribute to the spontaneous emission signal. The spatial resolution of STED is given by

$$d \approx (\lambda_{\text{STED}}/2) \times \text{NA} \times \sqrt{1 + I_m/I_s}, \qquad (5)$$

where λ_{STED} is the wavelength of the STED beam, NA is the numerical aperture of the objective lens, I_m is the maximum intensity of the STED beam, and I_s is the stimulated emission saturation intensity of NV. In this work, the NV in an SIL

fabricated directly in the bulk diamond was imaged with 2.4 nm accuracy.

Spin-RESOLFT [103,104] is a variant of STED. Unlike STED, which uses another ~775 nm light, Spin-RESOLFT requires a 532 nm laser only. In a Spin-RESOLFT measurement as sketched in Fig. 4(a), first, a Gaussian-shape light initializes the spin state of the NVs, and appropriate MWs prepare the spin states into a superposition. Then, a doughnut-shaped excitation laser is applied to erase all the information stored in the spin state of NVs but leaving the NVs in the central region unaffected. The spatial resolution of Spin-RESOLFT is given by

$$d \approx (\lambda/2) \times \text{NA} \times \sqrt{1 + \Gamma \tau_D}, \qquad (6)$$

where Γ is the rate of optical excitation of the spin, and τ_D is the duration of the doughnut-shaped beam that is only limited by the spin state relaxation time $T_1 > 100$ ms, which is much longer than the electronic excited state lifetime $\tau_{\text{FI}} \approx 12$ ns. A sensitivity of 250 nT/Hz$^{1/2}$ for the ac magnetic field was achieved with a resolution of 50 nm using XY8-k DD pulse sequence (where the sensitivity is 60 nT/Hz$^{1/2}$ in confocal mode with a single NV) [104].

CSD utilized the transition between NV⁻ and NV⁰ under laser excitation [105,106]. In CSD microscopy, a 532 nm Gaussian beam is applied to initialize the charge states of the NVs by converting NV⁰ into NV⁻. Then, a 637 nm (resonant with the ZPL of NV⁻) doughnut-shaped beam is used to ionize the NVs except for the central part. Last, a weak 0.1 mW
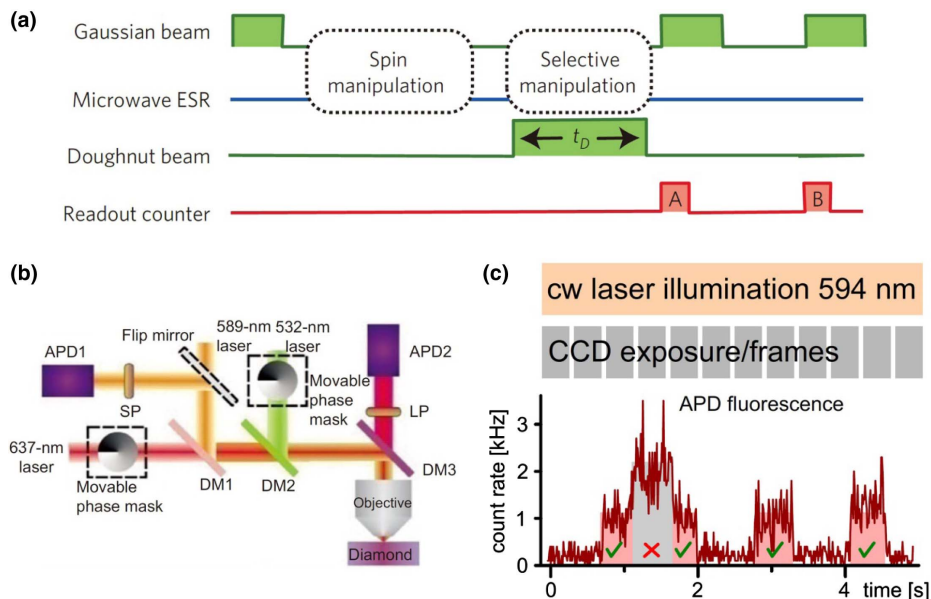

Fig. 4. Super-resolution microscopy techniques in NV⁻ magnetometry. (a) Schematic of the Spin-RESOLFT protocol used by Jaskula *et al.* The selective manipulation of the NV spin state is realized by a 532 nm doughnut beam. Reprinted with permission from Ref. [104]. Copyright 2017 Optical Society of America. (b) Schematic of the charge state depletion microscopy configuration. The 532 and 637 nm lasers were used to initialize and switch the charge state of NVs, and the 589 nm laser is for the charge state readout. The lasers and fluorescence emission were combined and split using three long-pass dichroic mirrors (DMs). The fluorescence of NV⁻ was detected by avalanche photodiode (APD2) with a long-pass filter (LP), and the fluorescence of NV⁰ was detected by APD1 with a short-pass filter (SP). Two phase masks were used to produce the doughnut-shaped laser beams. Reprinted with permission from Ref. [106]. Copyright 2015 Macmillan Publishers Ltd. (c) Exemplary fluorescence time trace recorded with an APD. Three count levels indicate 0–2 NVs are excited during each CCD exposure. Only those frames with one excited NV were chosen to reconstruct the super-resolution image. Adapted from Ref. [107].

589 nm (lower than the ZPL of NV^0) Gaussian beam, which selectively excites NV^- and leaves the charge state of NVs unaffected, is applied to readout the spin state of the NVs (this procedure is called rCSD) [106]; see Fig. 4(b). Switching the order and shape of 532 and 637 nm beams is also feasible (this procedure is called iCSD). In this case, the NV acts as a nanosized dark spot in the image, and better resolution can be achieved. In the work of Chen *et al.* [106], the authors realized a resolution of 4.1 nm with iCSD and 28.6 nm with rCSD, respectively.

In addition to those deterministic super-resolution microscopy methods mentioned above, stochastic super-resolution techniques such as single molecule location microscopy (SMLM) were also developed. The principle of SMLM is that, for a single emitter or few isolated emitters, it is possible to locate them with sub-100-nm precision using single emitter localization imaging reconstruction algorithms. In SMLM, 100–10,000 individual camera frames are taken, and in each frame, only a limited number of stochastically excited emitters are imaged. The image with sub-100-nm resolution is later reconstructed by determining the spatial positions of the individual emitters from their intensity intermittency in these camera frames. For NV in nanodiamonds, stochastic excitation was enabled by the blinking behavior of NV^- photoluminescence due to the surface defects and electron tunneling to near-surface defects, and SMLM was able to discern two NVs in a single nanodiamond 20 nm apart [108]. For NVs in bulk diamonds, a stochastic optical reconstruction microscopy (STORM) technique can be applied. In the work of Pfender *et al.* [107], a ~ 1 kW/cm^2 594 nm laser enables stochastic switching of NVs' charge state. The typical lifetimes of NV^- and NV^0 are ~ 2 s and ~ 20 s, which allows them to randomly excite 0–2 NVs during each CCD exposure; see Fig. 4(c). Eventually, a super-resolution of 27 nm with the spin manipulation and dc magnetic field sensitivity of 190 μT/Hz$^{1/2}$ were achieved in their work.

3. PROBING AFM/FM MATERIALS

Several studies on FM and AFM materials using NV^- magnetometry have been conducted by measuring static stray fields or magnetic excitations, as shown in the following. In this subsection, we will discuss the technical development for the study of spin texture and magnetic excitations.

A. Spin Texture Characterization

Micro- and nanoscale spin textures, such as DWs [81] and skyrmions [83], have recently become more attractive. The novel properties discovered in these structures indicate new physics as well as new possibilities for application in spintronics. Thus, experimental probes with high spatial resolution and minimum perturbation to the system are needed. Several techniques, including MFM [109,110], spin-polarized scanning tunneling microscopy [111,112], and X-ray magnetic dichroism [113,114], have been successfully applied in the study of spin structures. On the other hand, scanning probe NV^- magnetometry is an alternative noninvasive scheme that can directly image the absolute value of the magnetic field distributing near the sample surface [21,74,84]. Enabled by the high sensitivity

of NV^-, the stray field produced by nanoscale spin textures could be imaged quantitatively. By resolving the vector magnetic field distribution, accurate reconstruction of the underlying spin textures has also been demonstrated on various nanoscale spin structures [76,81,83].

For example, a magnetic DW is the interface separating two different magnetic domains and is a fundamental property of (anti-)ferromagnetism [115–117]. One of the exciting properties of the DW is the possibility of controlling its motion with current based on novel physical mechanisms, such as spin–transfer torque or spin–orbit torque [118–121]. These properties make it a potential candidate for non-volatile and high-speed memory devices [122–125]. However, the current-driven DW motion is highly related to the magnetic structure within DW and magnetic interactions [126,127]. Hence, characterization of the spin texture and investigation of the underlying interactions that stabilize DWs are of great importance. In many magnetic materials, the typical width of the DW is about 10–100 nm [81,128], depending mainly on the ratio of the exchange interaction and magnetic anisotropy energy [129]. The abrupt change of magnetization across DW results in a fairly large stray field, which is about ~ 1–10 mT, even at a distance of 100 nm above the sample surface [Fig. 5(a)] [81,82,128,130]. Scanning probe magnetometry with the NV^- sensor attached to the scanning tip can map the magnetic stray fields with high sensitivity and fine spatial resolution on magnetic thin films. Studies using scanning probe NV^- magnetometry carried out on tri-layer systems, such as Pt/Co/AlO$_x$ or Ta/CoFeB/MgO [81,82], as well as bi-layer magnetic insulator films TmIG/Pt on SGGG (111-oriented) [85], have successfully resolved the DW structure and confirmed the presence of interfacial Dzyaloshinskii–Moriya interaction (DMI) in ultrathin magnetic films. It was found that in the metallic tri-layer films, DMI stabilizes chiral DW. Interestingly, DMI can vary locally at the interface of magnetic insulators, signifying the importance of local probes [81,82,85].

Another newly discovered spin texture that attracts growing attention is the magnetic skyrmion. A magnetic skyrmion is a topological defect (around tens of nm) with a swirling spin configuration [131,132]. A topological number characterizing the winding of magnetization is invariant under continuous spin texture deformation [133]. Similar to DWs, skyrmions can be driven by electric current [134]. Therefore, it was proposed as a promising candidate for data storage in memory devices [135,136]. Detection of skyrmions requires magnetic sensitivity of ~ 1 mT with $\sim$nm spatial resolution with little magnetic perturbation [83,137]. Again, scanning probe NV^- magnetometry fits the needs for both conducting and insulating samples. Generally speaking, the reconstruction of spin texture from the stray field is an underconstrained inverse problem, which means the same field distribution can result from an infinite number of spin textures with different helicity and chirality [138]. However, one can uniquely deduce the spin texture with the *a priori* knowledge of the topological number. Dovzhenko *et al.* developed an algorithm to decompose the solution into superpositions of Néel-type and Bloch-type spin configuration and then calculated the topological number of these solutions
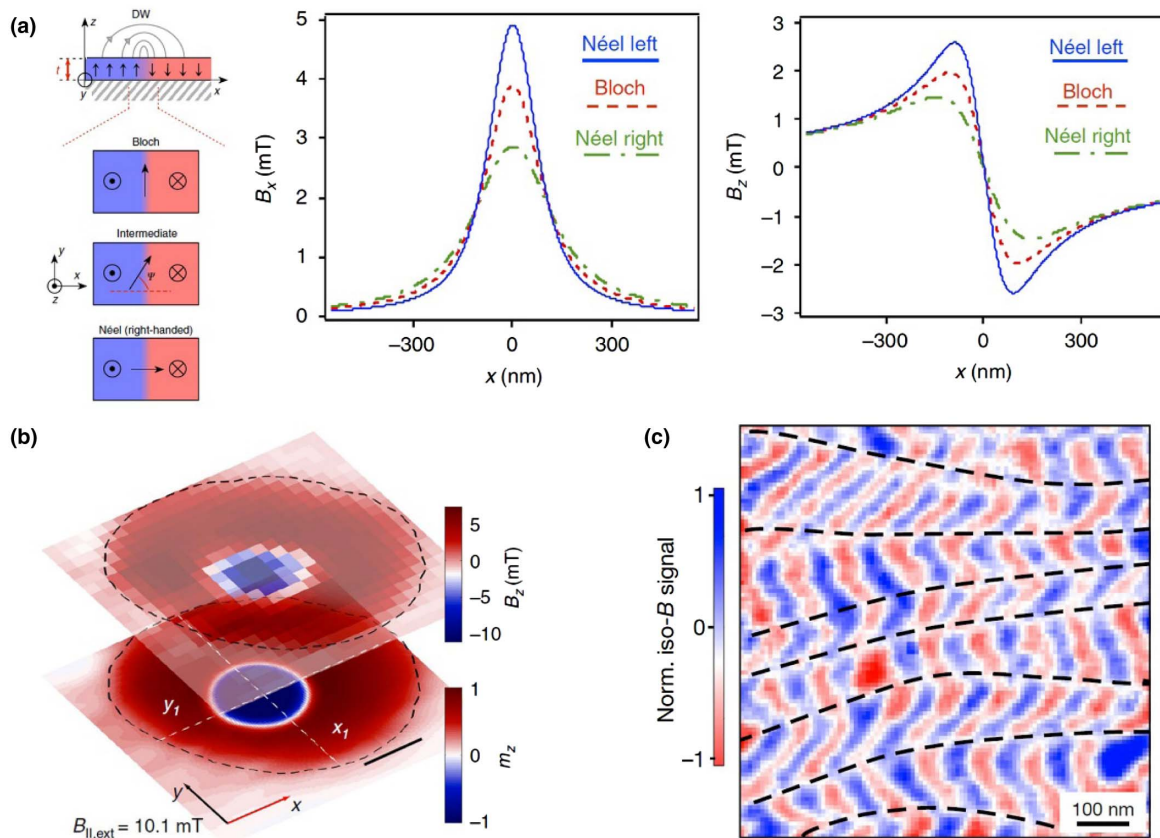
Fig. 5. Probing statistic magnetic structures in AFM/FM materials. (a) Determination of DW structure in ferromagnetic materials. Left, schematic side view of a DW in a perpendicularly magnetized film. The DW structure can be characterized by the angle Ψ of the internal magnetization indicated by the black arrows, while the stray field above the film represented by the gray arrows varies for different DW structures. Middle and right, calculated stray field components B_x and B_z at a distance $d = 120$ nm above the magnetic layer for DW of width ~ 20 nm, centered at $x = 0$. Reprinted with permission from Ref. [81]. Copyright 2015 Macmillan Publishers Ltd. (b) Reconstruction of magnetization of a skyrmion in an FM thin film. The upper sheet represents B_z component of the stray field for a skyrmion nucleated at the center of the magnetic disc, while the lower sheet is the reconstructed m_z component on the film. The black dashed lines represent the boundary of the disc. Scale bar, 300 nm. Reprinted with permission from Ref. [83]. Copyright 2018 Macmillan Publishers Ltd. (c) Real-space imaging of non-collinear antiferromagnetic order above the $BiFeO_3$ film while operating the NV$^-$ magnetometer in dual-iso-B imaging mode. The dual-iso-B signal $S = \mathrm{PL}(\nu_2) - \mathrm{PL}(\nu_1)$ corresponds to the difference in photoluminescence (PL) intensity for two fixed RF frequencies. The periodic variation of the magnetic stray field is caused by the cycloidal modulation of the spin order. The black dashed guidelines represent ferroelectric domain walls separating regions of different cycloidal propagation vector. Reprinted with permission from Ref. [76]. Copyright 2017 Macmillan Publishers Ltd.

[83]. By imposing the physical constraint that the topological number must be an integer, they managed to reconstruct the spin texture of a single skyrmion in multilayer magnetic films [Fig. 5(b)]. This result demonstrated the unique advantage of scanning probe NV$^-$ magnetometry in identifying complex nanoscale spin textures. Another approach to solving this underconstrained problem is to measure both the magnetization and its resulting stray magnetic fields. This can be realized by an imaging modality that performs NV$^-$ magnetometry and magneto-optic Kerr effect (MOKE) measurements at the same time [139].

The extension of scanning probe NV$^-$ magnetometry to study AFM spin texture is another landmark of NV$^-$ magnetometry. AFM materials are much more robust against magnetic field perturbations than FM counterparts and exhibit fast spin dynamics in the picosecond time scale [140–142]. Hence, they are considered promising candidates for next-generation ultrafast spintronics [143,144]. Imaging the spin

textures of AFM materials would provide information about the local order parameters. However, there exists a fundamental difficulty in probing AFM compared to FM materials. The spin configurations in AFM materials are nearly compensated with one another on a mesoscopic scale, leaving an extremely weak stray field out of the sample. Fortunately, at a nanoscale distance, the local magnetic field is not completely compensated near a DW or surface/interface with some residual surface magnetization. The highly-sensitive NV$^-$ magnetometry can sense the stray field with NV$^-$ centers placed a few nanometers away from the sample surface. Attempts using scanning probe NV$^-$ magnetometry to map AFM spin texture were first realized on non-collinear AFM materials, such as $BiFeO_3$ [76,86]. Later, it was also carried out on DWs/domain boundaries of thin films in AFM materials [145,146]. Being a multiferroic material, $BiFeO_3$ adopts a cycloidal spin configuration with a spatial period of ~ 64 nm, revealed by high-resolution neutron diffraction in bulk $BiFeO_3$. Gross *et al.* succeeded in imaging

the cycloidal spin texture in a BiFeO$_3$ thin film with scanning probe NV$^-$ magnetometry, extracting the spatial period of about 70 nm [Fig. 5(c)] [76]. The slight difference between the thin film and bulk can be explained by the strain imposed by the substrate [147]. However, quantitative reconstruction of spin configurations, as well as underlying DMI, requires additional knowledge about the chirality of the spin cycloid, and further investigation is needed. Interestingly, it was revealed by the scanning probe NV$^-$ magnetometry that non-collinear AFM features break the inversion symmetry, allowing real-time electric-field control with high efficiency [148–150].

A stray field close to the DW/domain boundary of collinear AFM materials is also within the detection limit of NV$^-$ magnetometry. Studies on collinear AFM thin films, such as granular Cr$_2$O$_3$ film [145,151] and van der Waals two-dimensional AFM material CrI$_3$ [146], have successfully demonstrated the capability of mapping domain boundaries using the scanning NV$^-$ sensors. For instance, Hedrich *et al.* investigated the 180° DW in a Cr$_2$O$_3$ film with scanning probe NV$^-$ magnetometry and revealed the pinning of the DW in the film [151]. These results show that scanning probe NV$^-$ magnetometry is a sensitive probe of static magnetic structures with high spatial resolution.

B. Magnetic Excitations

Magnetic excitations, such as spin-waves and magnetic noises, are one of the fundamental features in many correlated systems and serve as essential fingerprints for the understanding of material properties [152]. They also provide new degrees of freedom to actively control spins in data/information transfer or to offer alternative calculation resources for spintronics and quantum computing [153]. Probing magnetic excitations, as well as coherently manipulating these excitations and their interactions, is, thus, important to both fundamental interest and application.

As a quantum impurity, NV$^-$ center could be used to detect magnetic noise or directly probe a coherent ac magnetic field, as discussed in Section 2. The former could provide information about the excitation spectrum by measuring the noise spectrum

of the system, which is rooted in the fluctuation-dissipation theorem [154,155]. The latter, on the other hand, enables us to coherently drive magnetic excitations and study the interactions between such excitation and quantum impurity. It is worth noting that the noise-metrology using NV$^-$ is particularly attractive in the study of novel low-dimensional systems as it provides local probes for various magnetic excitations that are difficult to measure directly with neutron scattering [15] or muon spectroscopy [12]. Regarding the interactions with magnetic excitations, coherent driving of NV$^-$ qubit by magnetic excitations is widely used [156,157], providing inherent phase-sensitive detection. These studies pave the way for the future application of hybrid quantum devices.

For example, spin-wave, also known as magnon, is the bosonic magnetic excitation in ordered FM/AFM states [158], describing local disturbance, such as precession or nutation of spin, propagating across the lattice. Low dissipation spin transport can be achieved in magnetic insulators via spin-wave excitation. Thus, it is a promising candidate for the signal carrier in spintronics and hybrid quantum devices [153,159,160]. In FM materials, the excitation frequency of spin-wave lies in the ~GHz range [158]. Thus, coherent excitation and control of spin-wave in FM systems can be realized using microwave electric circuits, which has stimulated research on interference-based logic circuits, such as interconnects, transistors, and interferometers [161–163]. Imaging spin-wave transportation, especially in a phase-sensitive fashion, would be beneficial in characterizing these devices. Leading techniques for imaging coherent spin-waves include transmission X-ray microscopy [164,165], Brillouin light scattering [166], and Kerr microscopy [167]. All of these techniques rely on probing the spin-dependent optical response of the magnetic material. In comparison, NV$^-$ magnetometry images the microwave magnetic stray fields generated by coherent spin-waves. Specifically, the transition frequency of the NV$^-$ qubit is naturally in the GHz range and can be tuned continuously by an external bias magnetic field. Hence, one could adjust the NV$^-$ qubit transition frequency to match the spin-wave frequency. And then, the coherently excited spin-wave can be used to drive the Rabi
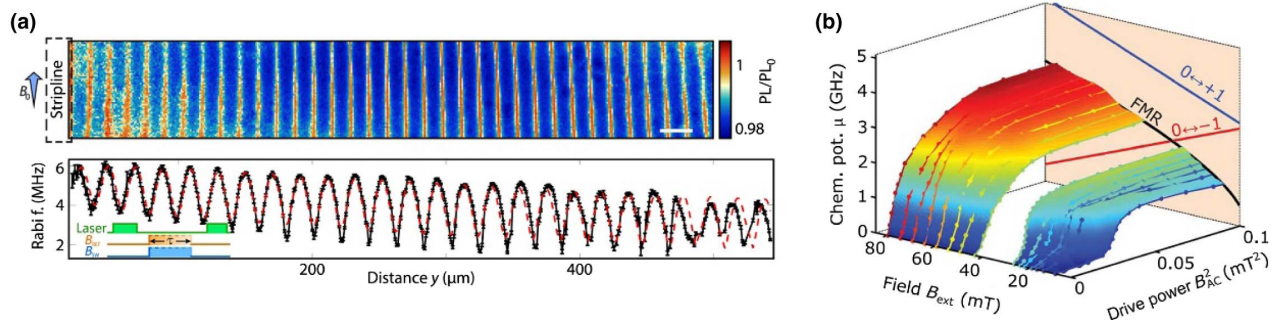

Fig. 6. Probing magnetic excitations in magnetic insulators. (a) Imaging coherent spin-waves. The pattern is generated by the interference between the stray field and an external spatially homogeneous field B_{REF} with the same frequency. Top, spatial ESR contrast at a bias field $B_0 = 25$ mT when a spin-wave of frequency equal to ESR frequency $\omega_{SW} = \omega_- = 2\pi \times 2.17$ GHz is excited by a microwave current in the stripline. Scale bar, 20 μm. Bottom, Rabi frequency $\omega_{Rabi}/2$ versus distance from the stripline when $\omega_{SW} = \omega_- = 2\pi \times 2.11$ GHz and $B_0 = 27$ mT. Red line, fitted Rabi frequency according to a model including the field of the stripline, the bonding wire, and the spin-waves. Inset, measurement sequence. Reprinted with permission from Ref. [157]. Copyright 2020 AAAS. (b) The spin chemical potential (μ) in YIG as a function of drive power (B_{AC}^2) and external bias field (B_{EXT}). μ saturates at the minimum of the magnon band set by the FMR frequency. Reprinted with permission from Ref. [168]. Copyright 2017 AAAS.

oscillation of the NV$^-$ qubit. To achieve phase-sensitive detection, another background microwave is usually applied to interfere with the oscillating magnetic field generated by spin-wave. The variation of interference across the sample gives rise to the difference in Rabi frequency that can be directly mapped in experiment. This method was first demonstrated on FM metal [156] and later on magnetic insulators, such as yttrium iron garnet (YIG) [Fig. 6(a)] [157]. Recent advances in fabricating high-quality magnetic insulator films have made these systems ideal platforms for studying magnon's propagation, interference, and scattering [157].

Besides coherent transport of spin-wave, novel magnon condensate emerging from interactions of magnons has also attracted much attention in the past decades. For example, with long-lived magnon and efficient magnon–magnon interaction, it is possible to realize Bose–Einstein condensate in high-quality magnetic insulators [169,170]. These novel states have distinct features in the magnetic excitation spectrum, and the relaxometry of NV$^-$ qubit, as mentioned in Section 2, can provide the spectrum by measuring the magnetic noise spectrum close to the sample [170–173]. Pioneering work carried out by Du *et al.* succeeded in tuning the chemical potential of YIG film and detecting the abrupt change of magnon chemical potential [Fig. 6(b)] via relaxometry of NV$^-$ in a diamond nano-rod on the surface of YIG [168]. Later, theoretical proposals have predicted NV$^-$ relaxometry as a powerful sensor to detect two-magnon scattering, hydrodynamics mode of magnon fluid, and chiral magnon–quantum impurity interactions [170–172,174].

4. PROBING SUPERCONDUCTORS

The application of NV$^-$ magnetometry in studying SCs has been mainly focused on the Meissner effect, as well as measuring the SC properties such as London penetration depth, superfluid density, and lower critical field [27,32,52,175–177].

Zero resistance and expelling of the magnetic flux (the Meissner effect) are known as concrete evidence of superconductivity in a material. The former relies on transport measurements, while the latter is characterized by diamagnetic responses. The traditional detection schemes for the Meissner effect, however, encounter difficulties in studying some novel

SCs. Some of these samples have limited size or are highly non-uniform in the mesoscopic scale [52,178]. Another category of SC samples is synthesized under high pressure [31,32]. Clearly, the techniques, including mutual inductance, superconducting quantum interference device, and microwave perturbation cavity, are difficult to implement. NV$^-$-based magnetometry, on the other hand, could provide alternative methods for the study of superconductivity.

As mentioned in Section 2, the spatial resolution of NV$^-$ magnetometry could easily reach the optical diffraction limit and sensitivity of $\sim 1~\mu T/Hz^{1/2}$, which is sufficient for measuring the Meissner effect of micrometer-scale SCs. Mapping of the Meissner effect using NV$^-$ magnetometry has been conducted on thin-film SCs, such as yttrium barium copper oxide (YBCO) [178], niobium [179], and $Bi_2Sr_2CaCu_2O_{8+\delta}$ (BSCCO) [52]. The magnetic field near the sample surface can, therefore, be spatially resolved to circumvent difficulties imposed by limited sample sizes. For example, Xu *et al.* prepared their sample by exfoliating BSCCO film directly on the diamond surface with an NV$^-$-enriched layer near the surface [52]. In their work, measurements on a micrometer-sized 33 nm film and a 125 nm bulk-like film of optimally doped BSCCO ($T_c = 91$ K) showed that the ac Meissner effect (or repulsion of ac magnetic field) sets in at 78 and 91 K, respectively [Figs. 7(a) and 7(b)], indicating that KT-like transition appears in the thin BSCCO film [52]. In addition, NV$^-$ magnetometry with wide-field imaging can resolve the vortices in type-II SCs and allows relatively high-speed imaging, which can be used for the study of flux pinning or as a universal tool to precisely measure the magnetic structures of thin films [180]. These studies established basic schemes for studying SCs using bulk diamond under cryogenic conditions and demonstrated that NV$^-$ magnetometry was a convenient tool for studying the magnetic response of SC from dc to the GHz regime on a scale of a few micrometers.

Another unique application of NV$^-$ sensors is to investigate superconductivity under high pressure. Here, NV$^-$ can be directly implanted near the surface of the diamond anvil cell and measure the local vector magnetic field [Fig. 8(a)] for pressures up to 60 GPa [29,30]. Attempts using NV$^-$ magnetometry to measure SC transition temperature were first demonstrated on
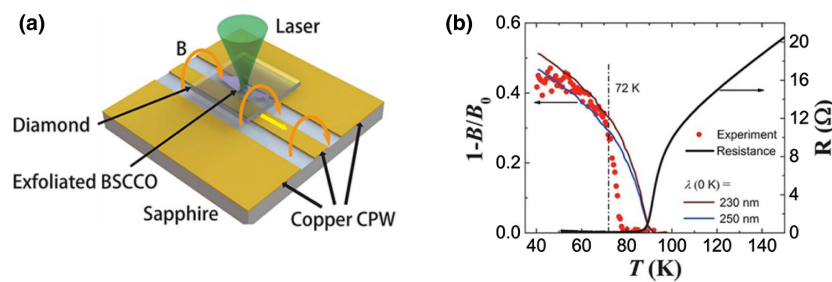

Fig. 7. Determination of superconductivity by NV$^-$ magnetometry. (a) Detection of ac Meissner effect on an ultrathin micron-size BSSCO film. The BSSCO flake was exfoliated on the diamond chip with NV$^-$ implanted at the surface. The yellow arrow represents the GHz current flowing in the central copper conductor. The orange arrows represent the direction of the microwave magnetic field. The 532 nm laser beam is normally incident. (b) Comparison of the measured (red dots) and calculated magnetic field (colored lines) expelled by the 33 nm thick BSSCO film versus temperature. The calculation is based on the two-fluid model, and the brown and blue curves show the results with λ assumed to be 230 and 250 nm, respectively. Resistance of the thin film versus temperature (black line) is shown for reference. (a), (b) Reprinted with permission from Ref. [52]. Copyright 2019 American Chemical Society.
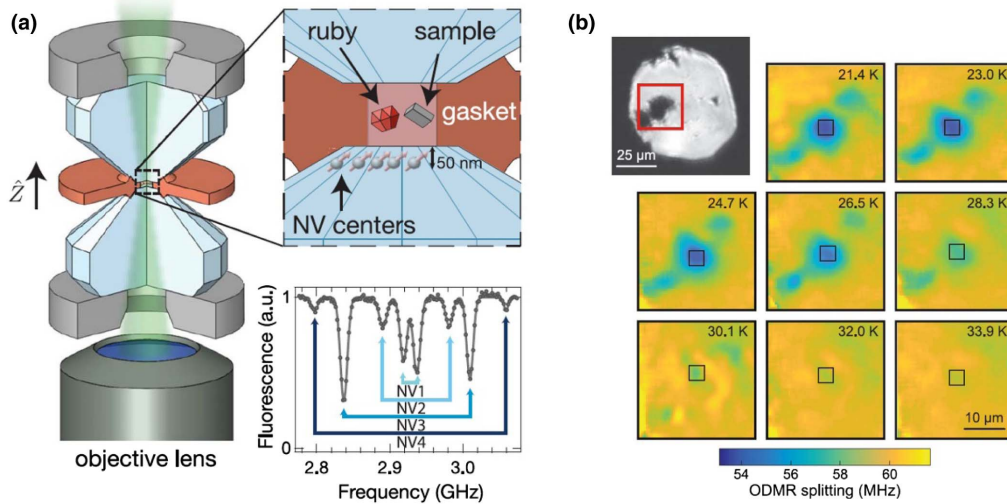
Fig. 8. Determination of superconductivity at high pressure by NV^- magnetometry. (a) Left, illustration of the diamond anvil cell (DAC) geometry. Two opposing anvils are compressed by a nonmagnetic steel cell and cubic boron nitride backing plates (gray). Top right, The DAC chamber loaded with the sample, a pressure-transmitting medium, and a single ruby microsphere for pressure calibration. A layer of NV^- centers near the surface is embedded into the diamond anvil at the bottom. Bottom right, a representative ODMR spectrum of an ensemble of NV^- centers. Four splitting groups are presented due to the four possible orientations of NV^- axes that result in different magnetic field projection cases. Reprinted with permission from Ref. [176]. Copyright 2019 AAAS. (b) Maps of the ODMR frequency splitting above the MgB_2 sample for different temperatures at a bias field $B_0 \approx 1.8$ mT. Below 30 K, expelling of the magnetic flux is observed and disappears above 30 K, indicating a transition from a superconducting state to a normal state. Top left, optical image of the sample. The red square marks the area where the ODMR splitting is mapped. Reprinted with permission from Ref. [31]. Copyright 2019 AAAS.

MgB_2 at 7 GPa [31] and $BaFe_2(As_{0.59}P_{0.41})_2$ at a few GPa [32] under a cryogenic environment. The repulsion of the magnetic field in MgB_2 at 7 GPa disappears at a temperature >30 K [Fig. 8(b)], consistent with T_c determined by transport measurement [181]. Meanwhile, in the studies of the $BaFe_2(As_{0.59}P_{0.41})_2$, the apparent change of the Zeeman splitting of the NV^- centers reflects that the superconducting phase transition happens near 20 K. It would be challenging but worthwhile to investigate how to implement NV^- magnetometry at pressure >100 GPa, which, if possible, would shed new light on the investigation of high-temperature superconductivity in various hydride compounds such as H_3S [182], LaH_{10} [183,184], UH_7 [185], and C–S–H systems [186].

In addition to determination of the onset of SC, NV^- is a powerful tool to characterize SCs by measuring the London penetration depth (λ) [27,175,187]. The London penetration depth is related to the superfluid density (n_s), which is one of the fundamental characteristics of an SC, through the well-known equation $\lambda^2 = mc^2/4\pi n_s e^2$ [188]. NV^- could measure λ in two ways. The first one is based on measurement of the lower critical field H_{c1}, beyond which the magnetic field starts to penetrate. H_{c1} is related to the London penetration depth and the coherence length (ξ) through the relation $H_{c1} = (\Phi_0/4\pi\lambda^2) \cdot [\ln(\lambda/\xi) + 0.497]$ [189], where $\Phi_0 = 2.07 \times 10^{-15}$ Wb is the magnetic flux quantum. ξ can be determined independently by measuring the upper critical field $H_{c2} = \Phi_0/2\pi\xi^2$. However, in practice, measurement of H_{c1} in the thin film or micro-sized sample is severely affected by extrinsic parameters, including variation of surface barriers and sample geometry [190–192]. The surface barrier prohibits

vortices from entering the internal volume of SCs [190]. Hence, the vortex would be pinned at the edge of the thin film after field penetration. Therefore, by probing the field penetration near the edge and considering the geometric conversion factor, one can deduce H_{c1} with better accuracy. This technique was applied to several SC films, such as optimally doped $Ba(Fe_{1-x}Co_x)_2As_2$, $x = 0.07$, stoichiometric $CaKFe_4As_4$, and the high-T_c YBCO [Fig. 9(a)] [175]. The London penetration depths evaluated from the H_{c1} values obtained are in good agreement with values in the literature.

The second approach is based on imaging vortices in SCs. Scanning probe NV^- magnetometry with ~10 nm spatial resolution and ~1 $\mu T/Hz^{1/2}$ DC sensitivity can fit the need [26,27,187]. Knowing the thickness of the SC film, the distance between NV and the sample, and the magnetic stray field generated by a vortex at a fixed height, one can deduce λ through fitting [193,194]. Vortices in $BaFe_2(As_{0.7}P_{0.3})_2$ film [Fig. 9(b)] [26] and $YBa_2Cu_3O_{7-\delta}$ film [Figs. 9(c) and 9(d)] [27,187] were measured using scanning probe NV^- magnetometry, and the penetration depth obtained agrees with previously reported values. These results demonstrate that scanning probe NV^- magnetometry is a powerful tool to address complex electronic systems through nanoscale magnetic field imaging.

5. PROBING METALS/SEMIMETALS/ SEMICONDUCTORS

NV^- magnetometry has also been applied to study metals/ semimetals/semiconductors, focusing mainly on the properties
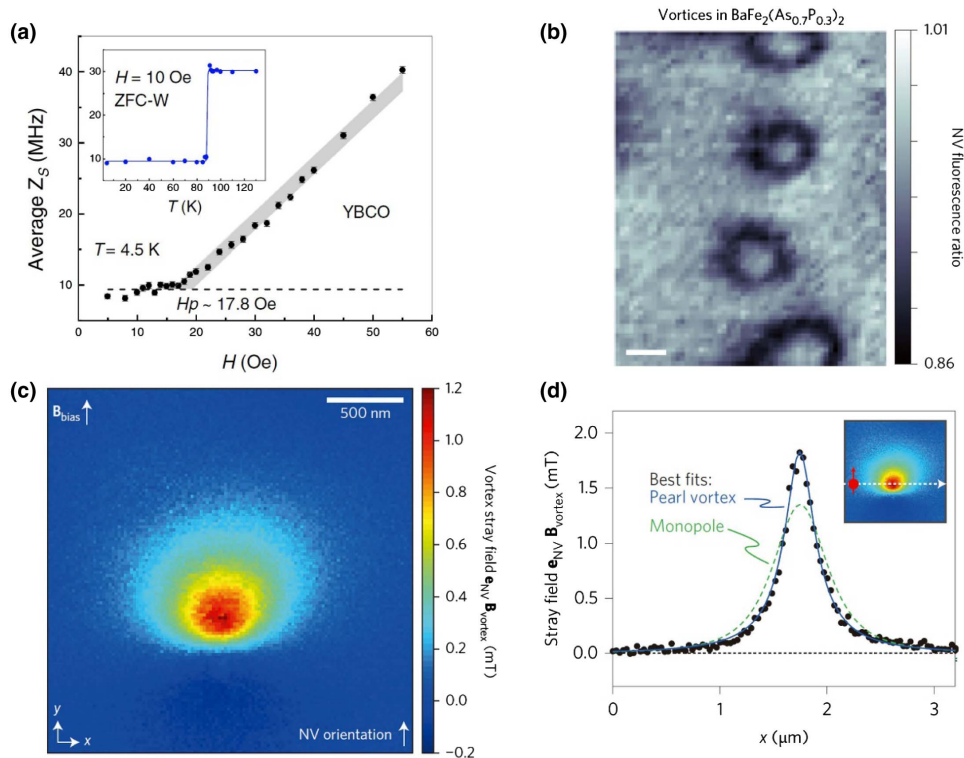
Fig. 9. Characteristic of superconductors investigated by NV^- magnetometry. (a) Measurements of the onset of the magnetic field penetration H_p on single crystal film of $YBa_2Cu_3O_{7-\delta}$. The inset shows the superconducting phase transition by measuring magnetic field screening in zero field cooling scheme, with transition temperature $T_c \approx 88$ K. Reprinted with permission from Ref. [175]. Copyright 2019 American Physical Society. (b) NV^- magnetometry image of vortices in the superconductor $BaFe_2(As_{0.7}P_{0.3})_2$ at $T = 6$ K. The vortices were formed by field cooling the sample to temperature below its T_c (~30 K) with an external field of 10 G. Dark areas in the image correspond to locations where the penetrated field has a magnitude of ~5.9 G (resonant with a 2862 MHz RF field) along the axis of the NV center. Scale bar, 400 nm. Reprinted with permission from Ref. [26]. Copyright 2016 Macmillan Publishers Ltd. (c) Image of the magnetic stray field emanating from a single vortex in a YBCO film with a thickness of ~100 nm, obtained with the scanning probe NV^- magnetometer. (d) Line profile of the magnetic field magnitude along a horizontal line above the YBCO film with a thickness of 150 nm, as shown in the insets. Blue and green dashed lines represent the best fittings to a Pearl vortex and a magnetic monopole. The bulk London penetration depth $\lambda = 251 \pm 14$ nm can be obtained from the fitting of Pearl vortex. (c) and (d) Reprinted with permission from Ref. [27]. Copyright 2016 Macmillan Publishers Ltd.

of electron conductivity below GHz. As the size of various modern devices approaches sub-micrometers or smaller, the contribution of edges or local defects becomes increasingly important [195–198]. Transport measurement is the most popular probe but cannot reveal the spatial variation of the electric response [199,200]. Current distribution can be resolved by measuring the local magnetic field generated by the current. Scanning Hall probes [201], magneto-optical imaging [202], and scanning SQUIDs [203] have shown the capability of mapping electric current with a spatial resolution varying from millimeter to sub-micrometer. Alternatively, NV^- magnetometry has the advantage of its nanoscale spatial resolution, high sensitivity, and tolerance of working temperature, as mentioned in Section 1. Imaging current flow in monolayer graphene [204,205], monolayer MoS_2 [206], Pt nanowire, and carbon nanotube [Fig. 10(a)] [97] has demonstrated the uniqueness of NV^- magnetometry. For instance, by attaching a diamond nanoparticle to the tip of an atomic force microscope with a single NV^- spin embedded, Chang *et al.* obtained a two-dimensional image of dc current density with sub-30-nm spatial resolution and ~1 μA sensitivity [97]. The nanoscale

resolution of the current density profile further enables the study of many other exotic transport phenomena, such as the hydrodynamics of viscous electron flow in graphene [Figs. 10(b) and 10(c)] [207]. In this work, current density with parabolic Poiseuille profile in a high-quality graphene sheet was observed for the first time by both a high-resolution scanning NV^- probe and a wide-field optical microscope with a bulk diamond chip. With improved magnetic field detection sensitivity as developed in literature [26,27,48,76,209–211], it is conceivable that NV^- magnetometry would soon be applied to the studies of electron transport in correlated materials [97].

Besides mapping of dc current distribution, the ability of NV^- to detect magnetic fluctuations can be used to measure thermally induced electrical currents or even non-equilibrium electronic phenomena. Thermally induced current fluctuations in metals, known as Johnson noise, are intrinsically related to the local conductivity. As mentioned in Section 2, current fluctuation generates broadband magnetic noise that can be sensed by the lifetime of NV^- spins in the GHz frequency window. In the work of Kolkowitz *et al.* [212], NV^- relaxometry showed
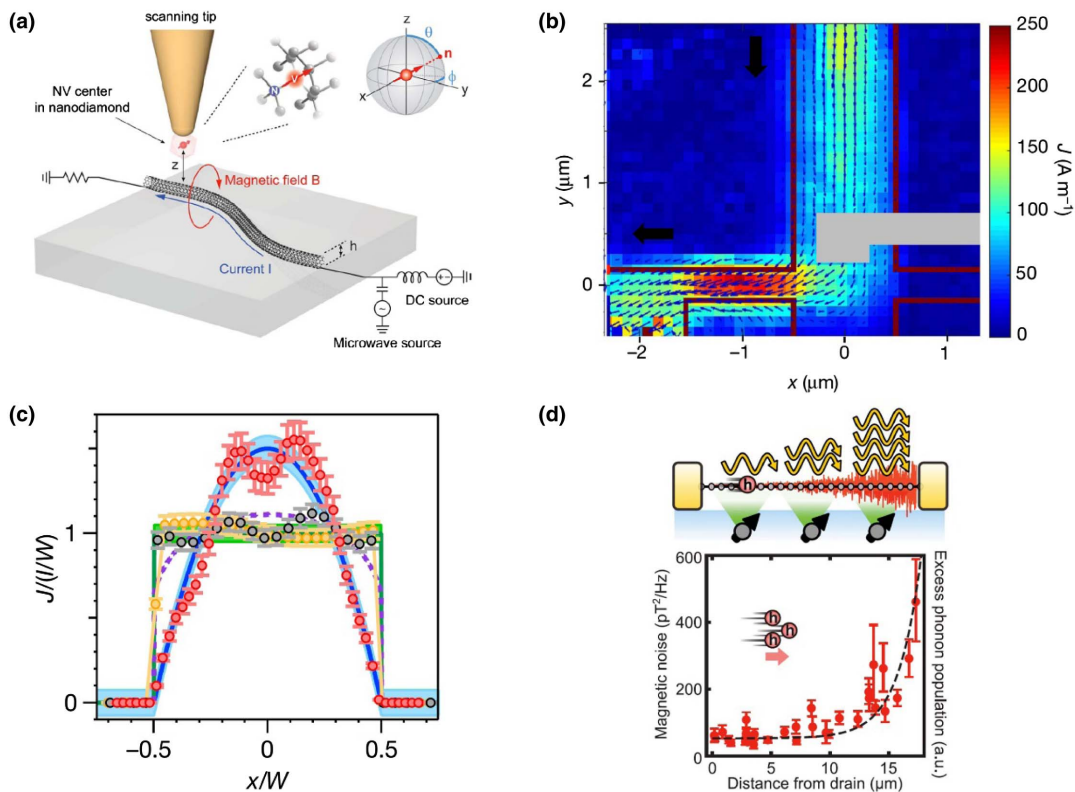
Fig. 10. Probing electron transport phenomena in metals/semimetals by NV^- magnetometry. (a) Illustration of mapping current density in the carbon nanotubes with the scanning NV^- magnetometer. A diamond nanoparticle hosting a single NV^- center is grafted onto the scanning tip of an atomic force microscope. During the detection, the nanoparticle is positioned at a distance less than 100 nm from a current-carrying carbon nanotube. The ESR frequency of the NV^- center is continuously monitored with the optical fluorescence collected by an objective (not shown). Reprinted with permission from Ref. [97]. Copyright 2017 American Chemical Society. (b) Mapping the viscous electron flow in graphene. The boundary of the graphene device is marked by red lines. Current is injected from the source (top), and the black arrows at the top and bottom left of the figure illustrate the current flow. 2D current density $\boldsymbol{J} = (J_x, J_y)$ reconstructed from the vector magnetic field detected by the wide-field NV^- magnetometer is plotted, with the direction indicated by black arrows and the amplitude indicated by color. The reconstructed flow pattern is consistent with the injected current. The gray area is covered by a metallic top-gate contact that obstructs light. (c) Current profiles across the graphene device reconstructed from the stray field measured by the scanning NV^- magnetometer. Current density $J_{y(x)}$ is normalized by the average 2D current density, where I is the total current and W is the width of the channel (1 μm for the graphene devices and 800 nm for the palladium electrode). Red dots, graphene at the charge-neutrality point (CNP); gray dots, palladium electrode; orange dots, low-mobility graphene. Blue (green) lines are calculated current density for ideal viscous (uniform) flow with 5% error band. (b) and (c) Reprinted with permission from Ref. [207]. Copyright 2020 Macmillan Publishers Ltd. (d) Spatial mapping of the local magnetic noise at current density $J = 0.18$ mA/μm and carrier density $n = 0.92 \times 10^{12}$ cm^{-2}. The spatial profile is consistent with the exponential growth of phonons due to Cerenkov amplification (cartoon, top). The dashed black curve shows the theoretically predicted excess phonon population (offset to account for background noise). a.u., arbitrary unit. Reprinted with permission from Ref. [208]. Copyright 2019 AAAS.

that the current fluctuation in polycrystalline silver films can be well described by the Drude model but is markedly suppressed in single crystal films where the ballistic motion of electrons dominates at a length scale below the electron mean free path [213]. Current fluctuation generated in a non-equilibrium system can also be probed by NV^- relaxometry. For example, suppression of conductivity and exponential growth of current fluctuations along the carrier-flow direction were observed in ultraclean graphene devices [Fig. 10(d)] [208]. These observations can be well explained by the emergence of electron–phonon Cerenkov instability at supersonic drift velocities, also known as Cerenkov amplification [214,215], which has long been theoretically explored as a method to produce high-frequency acoustic waves [216,217].

6. SUMMARY AND OUTLOOK

In this review, we have discussed the applications of NV^- magnetometry in probing condensed matter materials. Being point-like defects with remarkable coherent properties in diamond, NV^- centers are suitable sensors with high magnetic field sensitivity and high spatial resolution required to characterize materials under various working conditions. NV^- magnetometry has become a versatile and powerful tool in the studies of spin texture, magnetic excitation, the Meissner effect, and the non-invasive characterization of electron transport. It can provide unique information that is hardly accessible by conventional techniques.

Many opportunities lie beyond the applications described in this review. We argue that ac magnetic responses ranging from

~10 kHz to 10 GHz would benefit the characterization of the low dimensional quantum materials. Similar to the work of Xu *et al.*, by measuring the magnetic field distribution near the sample in ac driving magnetic field, one can deduce the magnetic susceptibility $\mu(\omega)$ for magnetic samples or conductivity $\sigma(\omega)$ for nonmagnetic samples, such as SC film or graphene sheet. In particular, if combined with a phase-sensitive detection scheme, for instance, heterodyne detection of ac magnetic field [54,218,219], such a technique would be useful in the investigation of phase transition of magnetic materials and SCs, as the imaginary part of $\mu(\omega)$ or $\sigma(\omega)$ would become significant near phase transition because of divergence of the relaxation time near T_c [188,220]. Meanwhile, one can take advantage of the long coherence of NV$^-$ in these detections with the DD method [22,221]. Also, theoretical proposals predict that vortex current distribution due to the hydrodynamics of electron flow would occur in, e.g., graphene if connected to ac current sources [222,223]. Such current patterns can also be resolved by measuring the ac magnetic field distribution near the sample surface, providing unique information for the understanding of electron hydrodynamics at low dimensions.

Exploring the relaxometry of NV$^-$ would also provide new opportunities for studying novel materials. As mentioned in Section 3.B, NV$^-$ relaxometry is predicted to be able to detect two-magnon scattering, hydrodynamics of magnon fluid, and chiral magnon–NV$^-$ interactions. Flebus *et al.* proposed that the DW motion in AFM materials could be characterized with NV$^-$ relaxometry [224]. Besides magnetic materials, Chatterjee *et al.* recently calculated the noise spectrum of superconducting films. They showed that measuring the noise spectrum would be a powerful noninvasive method to study KT-transition in two-dimensional superconducting thin films [225]. For low-dimensional materials, such as carbon nanotubes, NV$^-$ relaxometry would provide unique information about the spin-charge separation as predicted in Ref. [226].

We also noticed another interesting detection scheme proposed by Jiang and Wilczek [227]. They calculated the electromagnetic fluctuation-induced energy level splitting near the surface of a material and showed that such splitting is directly determined by, e.g., inversion and time-reversal symmetry of the underlying material. Therefore, detecting the NV$^-$ spin level splitting near novel materials would provide crucial evidence to determine, for instance, magnetic topological insulators and time-reversal broken superconducting films [227].

In summary, with continuous technological advances in the fabrication of NV$^-$ centers and the development of new sensing protocols and readout schemes, NV$^-$ magnetometry will find more exciting applications to condensed matter physics.

Disclosures. The authors declare no conflicts of interest.

Data Availability. Data underlying the results presented in this paper are not publicly available at this time but may be obtained from the authors upon reasonable request.

[†]These authors contributed equally to this paper.

REFERENCES

1. Q. Si, R. Yu, and E. Abrahams, "High-temperature superconductivity in iron pnictides and chalcogenides," Nat. Rev. Mater. **1**, 16017 (2016).
2. L. J. Zhang, Y. C. Wang, J. Lv, and Y. M. Ma, "Materials discovery at high pressures," Nat. Rev. Mater. **2**, 17005 (2017).
3. L. P. Gor'kov and V. Z. Kresin, "Colloquium: high pressure and road to room temperature superconductivity," Rev. Mod. Phys. **90**, 011001 (2018).
4. A. K. Geim and I. V. Grigorieva, "Van der Waals heterostructures," Nature **499**, 419–425 (2013).
5. K. S. Burch, D. Mandrus, and J. G. Park, "Magnetism in two-dimensional van der Waals materials," Nature **563**, 47–52 (2018).
6. Y. Tokura, K. Yasuda, and A. Tsukazaki, "Magnetic topological insulators," Nat. Rev. Phys. **1**, 126–143 (2019).
7. N. Nagaosa, T. Morimoto, and Y. Tokura, "Transport, magnetic and optical properties of Weyl materials," Nat. Rev. Mater. **5**, 621–636 (2020).
8. S. D. Bader and S. S. P. Parkin, "Spintronics," Annu. Rev. Condens. Matter Phys. **1**, 71–88 (2010).
9. P. Zubko, S. Gariglio, M. Gabay, P. Ghosez, and J. M. Triscone, "Interface physics in complex oxide heterostructures," Annu. Rev. Condens. Matter Phys. **2**, 141–165 (2011).
10. C. Granata and A. Vettoliere, "Nano superconducting quantum interference device: a powerful tool for nanoscale investigations," Phys. Rep. **614**, 1–69 (2016).
11. F. Casola, T. van der Sar, and A. Yacoby, "Probing condensed matter physics with magnetometry based on nitrogen-vacancy centres in diamond," Nat. Rev. Mater. **3**, 17088 (2018).
12. L. Nuccio, L. Schulz, and A. J. Drew, "Muon spin spectroscopy: magnetism, soft matter and the bridge between the two," J. Phys. D **47**, 473001 (2014).
13. M. H. Levitt, *Spin Dynamics: Basics of Nuclear Magnetic Resonance* (Wiley, 2013).
14. M. C. D. Tayler, T. Theis, T. F. Sjolander, J. W. Blanchard, A. Kentner, S. Pustelny, A. Pines, and D. Budker, "Invited review article: instrumentation for nuclear magnetic resonance in zero and ultralow magnetic field," Rev. Sci. Instrum. **88**, 091101 (2017).
15. S. Mühlbauer, D. Honecker, É. A. Périgo, F. Bergner, S. Disch, A. Heinemann, S. Erokhin, D. Berkov, C. Leighton, M. R. Eskildsen, and A. Michels, "Magnetic small-angle neutron scattering," Rev. Mod. Phys. **91**, 015004 (2019).
16. D. Rugar, R. Budakian, H. J. Mamin, and B. W. Chui, "Single spin detection by magnetic resonance force microscopy," Nature **430**, 329–332 (2004).
17. O. Kazakova, R. Puttock, C. Barton, H. Corte-Leon, M. Jaafar, V. Neu, and A. Asenjo, "Frontiers of magnetic force microscopy," J. Appl. Phys. **125**, 060901 (2019).
18. H. Suderow, I. Guillamon, J. G. Rodrigo, and S. Vieira, "Imaging superconducting vortex cores and lattices with a scanning tunneling microscope," Supercond. Sci. Technol. **27**, 063001 (2014).
19. L. Rondin, J. P. Tetienne, T. Hingant, J. F. Roch, P. Maletinsky, and V. Jacques, "Magnetometry with nitrogen-vacancy defects in diamond," Rep. Prog. Phys. **77**, 056503 (2014).
20. J. R. Maze, P. L. Stanwix, J. S. Hodges, S. Hong, J. M. Taylor, P. Cappellaro, L. Jiang, M. V. G. Dutt, E. Togan, A. S. Zibrov, A. Yacoby, R. L. Walsworth, and M. D. Lukin, "Nanoscale magnetic sensing with an individual electronic spin in diamond," Nature **455**, 644–647 (2008).
21. G. Balasubramanian, I. Y. Chan, R. Kolesov, M. Al-Hmoud, J. Tisler, C. Shin, C. Kim, A. Wojcik, P. R. Hemmer, A. Krueger, T. Hanke, A. Leitenstorfer, R. Bratschitsch, F. Jelezko, and J. Wrachtrup,

"Nanoscale imaging magnetometry with diamond spins under ambient conditions," Nature **455**, 648–651 (2008).

22. J. M. Taylor, P. Cappellaro, L. Childress, L. Jiang, D. Budker, P. R. Hemmer, A. Yacoby, R. Walsworth, and M. D. Lukin, "High-sensitivity diamond magnetometer with nanoscale resolution," Nat. Phys. **4**, 810–816 (2008).

23. M. S. Grinolds, S. Hong, P. Maletinsky, L. Luan, M. D. Lukin, R. L. Walsworth, and A. Yacoby, "Nanoscale magnetic imaging of a single electron spin under ambient conditions," Nat. Phys. **9**, 215–219 (2013).

24. A. O. Sushkov, I. Lovchinsky, N. Chisholm, R. L. Walsworth, H. Park, and M. D. Lukin, "Magnetic resonance detection of individual proton spins using quantum reporters," Phys. Rev. Lett. **113**, 197601 (2014).

25. M. S. Grinolds, M. Warner, K. De Greve, Y. Dovzhenko, L. Thiel, R. L. Walsworth, S. Hong, P. Maletinsky, and A. Yacoby, "Subnanometre resolution in three-dimensional magnetic resonance imaging of individual dark spins," Nat. Nanotechnol. **9**, 279–284 (2014).

26. M. Pelliccione, A. Jenkins, P. Ovartchaiyapong, C. Reetz, E. Emmanouilidou, N. Ni, and A. C. B. Jayich, "Scanned probe imaging of nanoscale magnetism at cryogenic temperatures with a single-spin quantum sensor," Nat. Nanotechnol. **11**, 700–705 (2016).

27. L. Thiel, D. Rohner, M. Ganzhorn, P. Appel, E. Neu, B. Mueller, R. Kleiner, D. Koelle, and P. Maletinsky, "Quantitative nanoscale vortex imaging using a cryogenic quantum magnetometer," Nat. Nanotechnol. **11**, 677–681 (2016).

28. G.-Q. Liu, X. Feng, N. Wang, Q. Li, and R.-B. Liu, "Coherent quantum control of nitrogen-vacancy center spins near 1000 kelvin," Nat. Commun. **10**, 1344 (2019).

29. M. W. Doherty, V. V. Struzhkin, D. A. Simpson, L. P. McGuinness, Y. Meng, A. Stacey, T. J. Karle, R. J. Hemley, N. B. Manson, L. C. L. Hollenberg, and S. Prawer, "Electronic properties and metrology applications of the diamond NV⁻ center under pressure," Phys. Rev. Lett. **112**, 047601 (2014).

30. L. G. Steele, M. Lawson, M. Onyszczak, B. T. Bush, Z. Mei, A. P. Dioguardi, J. King, A. Parker, A. Pines, S. T. Weir, W. Evans, K. Visbeck, Y. K. Vohra, and N. J. Curro, "Optically detected magnetic resonance of nitrogen vacancies in a diamond anvil cell using designer diamond anvils," Appl. Phys. Lett. **111**, 221903 (2017).

31. M. Lesik, T. Plisson, L. Toraille, J. Renaud, F. Occelli, M. Schmidt, O. Salord, A. Delobbe, T. Debuisschert, L. Rondin, P. Loubeyre, and J. F. Roch, "Magnetic measurements on micrometer-sized samples under high pressure using designed NV centers," Science **366**, 1359–1362 (2019).

32. K. Y. Yip, K. O. Ho, K. Y. Yu, Y. Chen, W. Zhang, S. Kasahara, Y. Mizukami, T. Shibauchi, Y. Matsuda, S. K. Goh, and S. Yang, "Measuring magnetic field texture in correlated electron systems under extreme conditions," Science **366**, 1355–1359 (2019).

33. M. W. Doherty, N. B. Manson, P. Delaney, F. Jelezko, J. Wrachtrup, and L. C. L. Hollenberg, "The nitrogen-vacancy colour centre in diamond," Phys. Rep. **528**, 1–45 (2013).

34. R. Schirhagl, K. Chang, M. Loretz, and C. L. Degen, "Nitrogen-vacancy centers in diamond: nanoscale sensors for physics and biology," Annu. Rev. Phys. Chem. **65**, 83–105 (2014).

35. L. Childress, R. Walsworth, and M. Lukin, "Atom-like crystal defects: from quantum computers to biological sensors," Phys. Today **67**, 38–43 (2014).

36. J. F. Barry, J. M. Schloss, E. Bauch, M. J. Turner, C. A. Hart, L. M. Pham, and R. L. Walsworth, "Sensitivity optimization for NV-diamond magnetometry," Rev. Mod. Phys. **92**, 015004 (2020).

37. N. F. Ramsey, "A molecular beam resonance method with separated oscillating fields," Phys. Rev. **78**, 695–699 (1950).

38. B. J. Shields, Q. P. Unterreithmeier, N. P. de Leon, H. Park, and M. D. Lukin, "Efficient readout of a single spin state in diamond via spin-to-charge conversion," Phys. Rev. Lett. **114**, 136402 (2015).

39. V. V. Dobrovitski, A. E. Feiguin, D. D. Awschalom, and R. Hanson, "Decoherence dynamics of a single spin versus spin ensemble," Phys. Rev. B **77**, 245212 (2008).

40. R. de Sousa, "Electron spin as a spectrometer of nuclear-spin noise and other fluctuations," in _Electron Spin Resonance and Related Phenomena in Low-Dimensional Structures_, M. Fanciulli, ed. (Springer Berlin Heidelberg, 2009), pp. 183–220.

41. L. T. Hall, J. H. Cole, and L. C. L. Hollenberg, "Analytic solutions to the central-spin problem for nitrogen-vacancy centers in diamond," Phys. Rev. B **90**, 075201 (2014).

42. G. de Lange, T. van der Sar, M. Blok, Z. H. Wang, V. Dobrovitski, and R. Hanson, "Controlling the quantum dynamics of a mesoscopic spin bath in diamond," Sci. Rep. **2**, 382 (2012).

43. H. S. Knowles, D. M. Kara, and M. Atature, "Observing bulk diamond spin coherence in high-purity nanodiamonds," Nat. Mater. **13**, 21–25 (2014).

44. E. Bauch, C. A. Hart, J. M. Schloss, M. J. Turner, J. F. Barry, P. Kehayias, S. Singh, and R. L. Walsworth, "Ultralong dephasing times in solid-state spin ensembles via quantum control," Phys. Rev. X **8**, 031025 (2018).

45. P. Jamonneau, M. Lesik, J. P. Tetienne, I. Alvizu, L. Mayer, A. Dreau, S. Kosen, J. F. Roch, S. Pezzagna, J. Meijer, T. Teraji, Y. Kubo, P. Bertet, J. R. Maze, and V. Jacques, "Competition between electric field and magnetic field noise in the decoherence of a single spin in diamond," Phys. Rev. B **93**, 024305 (2016).

46. J. M. Schloss, J. F. Barry, M. J. Turner, and R. L. Walsworth, "Simultaneous broadband vector magnetometry using solid-state spins," Phys. Rev. Appl. **10**, 034044 (2018).

47. K. Fang, V. M. Acosta, C. Santori, Z. Huang, K. M. Itoh, H. Watanabe, S. Shikata, and R. G. Beausoleil, "High-sensitivity magnetometry based on quantum beats in diamond nitrogen-vacancy centers," Phys. Rev. Lett. **110**, 130802 (2013).

48. G. de Lange, Z. H. Wang, D. Riste, V. V. Dobrovitski, and R. Hanson, "Universal dynamical decoupling of a single solid-state spin from a spin bath," Science **330**, 60–63 (2010).

49. L. M. Pham, N. Bar-Gill, C. Belthangady, D. Le Sage, P. Cappellaro, M. D. Lukin, A. Yacoby, and R. L. Walsworth, "Enhanced solid-state multispin metrology using dynamical decoupling," Phys. Rev. B **86**, 045214 (2012).

50. P. Appel, M. Ganzhorn, E. Neu, and P. Maletinsky, "Nanoscale microwave imaging with a single electron spin in diamond," New J. Phys. **17**, 112001 (2015).

51. I. Jakobi, P. Neumann, Y. Wang, D. B. R. Dasari, F. El Hallak, M. A. Bashir, M. Markham, A. Edmonds, D. Twitchen, and J. Wrachtrupu, "Measuring broadband magnetic fields on the nanoscale using a hybrid quantum register," Nat. Nanotechnol. **12**, 67–72 (2017).

52. Y. Xu, Y. Yu, Y. Y. Hui, Y. Su, J. Cheng, H.-C. Chang, Y. Zhang, Y. R. Shen, and C. Tiang, "Mapping dynamical magnetic responses of ultrathin micron-size superconducting films using nitrogen-vacancy centers in diamond," Nano Lett. **19**, 5697–5702 (2019).

53. T. Joas, A. M. Waeber, G. Braunbeck, and F. Reinhard, "Quantum sensing of weak radio-frequency signals by pulsed Mollow absorption spectroscopy," Nat. Commun. **8**, 964 (2017).

54. J. Meinel, V. Vorobyov, B. Yavkin, D. Dasari, H. Sumiya, S. Onoda, J. Isoya, and J. Wrachtrup, "Heterodyne sensing of microwaves with a quantum sensor," Nat. Commun. **12**, 2737 (2021).

55. D. A. Hopper, R. R. Grote, A. L. Exarhos, and L. C. Bassett, "Near-infrared-assisted charge control and spin readout of the nitrogen-vacancy center in diamond," Phys. Rev. B **94**, 241201 (2016).

56. A. Ariyaratne, D. Bluvstein, B. A. Myers, and A. C. B. Jayich, "Nanoscale electrical conductivity imaging using a nitrogen-vacancy center in diamond," Nat. Commun. **9**, 2406 (2018).

57. J. C. Jaskula, B. J. Shields, E. Bauch, M. D. Lukin, A. S. Trifonov, and R. L. Walsworth, "Improved quantum sensing with a single solid-state spin via spin-to-charge conversion," Phys. Rev. Appl. **11**, 064003 (2019).

58. D. A. Hopper, R. R. Grote, S. M. Parks, and L. C. Bassett, "Amplified sensitivity of nitrogen-vacancy spins in nanodiamonds using all-optical charge readout," ACS Nano **12**, 4678–4686 (2018).

59. H. Jayakumar, S. Dhomkar, J. Henshaw, and C. A. Meriles, "Spin readout via spin-to-charge conversion in bulk diamond nitrogen-vacancy ensembles," Appl. Phys. Lett. **113**, 122404 (2018).

60. K. Beha, A. Batalov, N. B. Manson, R. Bratschitsch, and A. Leitenstorfer, "Optimum photoluminescence excitation and recharging cycle of single nitrogen-vacancy centers in ultrapure diamond," Phys. Rev. Lett. **109**, 097404 (2012).

61. D. Le Sage, L. M. Pham, N. Bar-Gill, C. Belthangady, M. D. Lukin, A. Yacoby, and R. L. Walsworth, "Efficient photon detection from color centers in a diamond optical waveguide," Phys. Rev. B **85**, 121202 (2012).

62. Z. M. Ma, S. W. Zhang, Y. P. Fu, H. Yuan, Y. B. Shi, J. Gao, L. Qin, J. Tang, J. Liu, and Y. J. Li, "Magnetometry for precision measurement using frequency-modulation microwave combined efficient photon-collection technique on an ensemble of nitrogen-vacancy centers in diamond," Opt. Express **26**, 382–390 (2018).

63. T. Wolf, P. Neumann, K. Nakamura, H. Sumiya, T. Ohshima, J. Isoya, and J. Wrachtrup, "Subpicotesla diamond magnetometry," Phys. Rev. X **5**, 041001 (2015).

64. N. Hedrich, D. Rohner, M. Batzer, P. Maletinsky, and B. J. Shields, "Parabolic diamond scanning probes for single-spin magnetic field imaging," Phys. Rev. Appl. **14**, 064007 (2020).

65. L. Z. Li, E. H. Chen, J. B. Zheng, S. L. Mouradian, F. Dolde, T. Schroder, S. Karaveli, M. L. Markham, D. J. Twitchen, and D. Englund, "Efficient photon collection from a nitrogen vacancy center in a circular bullseye grating," Nano Lett. **15**, 1493–1497 (2015).

66. J. T. Choy, B. J. M. Hausmann, T. M. Babinec, I. Bulu, M. Khan, P. Maletinsky, A. Yacoby, and M. Loncar, "Enhanced single-photon emission from a diamond-silver aperture," Nat. Photonics **5**, 738–743 (2011).

67. J. P. Hadden, J. P. Harrison, A. C. Stanley-Clarke, L. Marseglia, Y. L. D. Ho, B. R. Patton, J. L. O'Brien, and J. G. Rarity, "Strongly enhanced photon collection from diamond defect centers under microfabricated integrated solid immersion lenses," Appl. Phys. Lett. **97**, 241901 (2010).

68. S. Castelletto, J. P. Harrison, L. Marseglia, A. C. Stanley-Clarke, B. C. Gibson, B. A. Fairchild, J. P. Hadden, Y. L. D. Ho, M. P. Hiscocks, K. Ganesan, S. T. Huntington, F. Ladouceur, A. D. Greentree, S. Prawer, J. L. O'Brien, and J. G. Rarity, "Diamond-based structures to collect and guide light," New J. Phys. **13**, 025020 (2011).

69. M. Jamali, I. Gerhardt, M. Rezai, K. Frenner, H. Fedder, and J. Wrachtrup, "Microscopic diamond solid-immersion-lenses fabricated around single defect centers by focused ion beam milling," Rev. Sci. Instrum. **85**, 123703 (2014).

70. Q. Zhang, Y. H. Guo, W. T. Ji, M. Q. Wang, J. Yin, F. Kong, Y. H. Lin, C. M. Yin, F. Z. Shi, Y. Wang, and J. F. Du, "High-fidelity single-shot readout of single electron spin in diamond with spin-to-charge conversion," Nat. Commun. **12**, 1529 (2021).

71. K. M. C. Fu, C. Santori, P. E. Barclay, I. Aharonovich, S. Prawer, N. Meyer, A. M. Holm, and R. G. Beausoleil, "Coupling of nitrogen-vacancy centers in diamond to a GaP waveguide," Appl. Phys. Lett. **93**, 234107 (2008).

72. D. Riedel, D. Rohner, M. Ganzhorn, T. Kaldewey, P. Appel, E. Neu, R. J. Warburton, and P. Maletinsky, "Low-loss broadband antenna for efficient photon collection from a coherent spin in diamond," Phys. Rev. Appl. **2**, 064011 (2014).

73. B. J. M. Hausmann, M. Khan, Y. N. Zhang, T. M. Babinec, K. Martinick, M. McCutcheon, P. R. Hemmer, and M. Loncar, "Fabrication of diamond nanowires for quantum information processing applications," Diamond Relat. Mater. **19**, 621–629 (2010).

74. P. Maletinsky, S. Hong, M. S. Grinolds, B. Hausmann, M. D. Lukin, R. L. Walsworth, M. Loncar, and A. Yacoby, "A robust scanning diamond sensor for nanoscale imaging with single nitrogen-vacancy centres," Nat. Nanotechnol. **7**, 320–324 (2012).

75. T. X. Zhou, R. J. Stohr, and A. Yacoby, "Scanning diamond NV center probes compatible with conventional AFM technology," Appl. Phys. Lett. **111**, 163106 (2017).

76. I. Gross, W. Akhtar, V. Garcia, L. J. Martinez, S. Chouaieb, K. Garcia, C. Carretero, A. Barthelemy, P. Appel, P. Maletinsky, J. V. Kim, J. Y. Chauleau, N. Jaouen, M. Viret, M. Bibes, S. Fusil, and V. Jacques, "Real-space imaging of non-collinear antiferromagnetic order with a single-spin magnetometer," Nature **549**, 252–256 (2017).

77. D. A. Broadway, S. E. Lillie, S. C. Scholten, D. Rohner, N. Dontschuk, P. Maletinsky, J. P. Tetienne, and L. C. L. Hollenberg, "Improved current density and magnetization reconstruction through vector magnetic field measurements," Phys. Rev. Appl. **14**, 024076 (2020).

78. B. A. Myers, A. Das, M. C. Dartiailh, K. Ohno, D. D. Awschalom, and A. C. B. Jayich, "Probing surface noise with depth-calibrated spins in diamond," Phys. Rev. Lett. **113**, 027602 (2014).

79. B. A. Myers, A. Ariyaratne, and A. C. B. Jayich, "Double-quantum spin-relaxation limits to coherence of near-surface nitrogen-vacancy centers," Phys. Rev. Lett. **118**, 197201 (2017).

80. J. F. Barry, M. J. Turner, J. M. Schloss, D. R. Glenn, Y. Song, M. D. Lukin, H. Park, and R. L. Walsworth, "Optical magnetic detection of single-neuron action potentials using quantum defects in diamond," Proc. Natl. Acad. Sci. USA **113**, 14133–14138 (2016).

81. J. P. Tetienne, T. Hingant, L. J. Martinez, S. Rohart, A. Thiaville, L. H. Diez, K. Garcia, J. P. Adam, J. V. Kim, J. F. Roch, I. M. Miron, G. Gaudin, L. Vila, B. Ocker, D. Ravelosona, and V. Jacques, "The nature of domain walls in ultrathin ferromagnets revealed by scanning nanomagnetometry," Nat. Commun. **6**, 6733 (2015).

82. I. Gross, L. J. Martinez, J. P. Tetienne, T. Hingant, J. F. Roch, K. Garcia, R. Soucaille, J. P. Adam, J. V. Kim, S. Rohart, A. Thiaville, J. Torrejon, M. Hayashi, and V. Jacques, "Direct measurement of interfacial Dzyaloshinskii-Moriya interaction in X|CoFeB|MgO heterostructures with a scanning NV magnetometer (X=Ta, TaN, and W)," Phys. Rev. B **94**, 064413 (2016).

83. Y. Dovzhenko, F. Casola, S. Schlotter, T. X. Zhou, F. Buttner, R. L. Walsworth, G. S. D. Beach, and A. Yacoby, "Magnetostatic twists in room-temperature skyrmions explored by nitrogen-vacancy center spin texture reconstruction," Nat. Commun. **9**, 2712 (2018).

84. L. Rondin, J. P. Tetienne, P. Spinicelli, C. Dal Savio, K. Karrai, G. Dantelle, A. Thiaville, S. Rohart, J. F. Roch, and V. Jacques, "Nanoscale magnetic field mapping with a single spin scanning probe magnetometer," Appl. Phys. Lett. **100**, 153118 (2012).

85. S. Velez, J. Schaab, M. S. Wornle, M. Muller, E. Gradauskaite, P. Welter, C. Gutgsell, C. Nistor, C. L. Degen, M. Trassin, M. Fiebig, and P. Gambardella, "High-speed domain wall racetracks in a magnetic insulator," Nat. Commun. **10**, 4750 (2019).

86. A. Haykal, J. Fischer, W. Akhtar, J. Y. Chauleau, D. Sando, A. Finco, F. Godel, Y. A. Birkholzer, C. Carretero, N. Jaouen, M. Bibes, M. Viret, S. Fusil, V. Jacques, and V. Garcia, "Antiferromagnetic textures in BiFeO₃ controlled by strain and electric field," Nat. Commun. **11**, 1704 (2020).

87. M. Chipaux, A. Tallaire, J. Achard, S. Pezzagna, J. Meijer, V. Jacques, J. F. Roch, and T. Debuisschert, "Magnetic imaging with an ensemble of nitrogen vacancy-centers in diamond," Eur. Phys. J. D **69**, 166 (2015).

88. K. Sasaki, E. E. Kleinsasser, Z. Y. Zhu, W. D. Li, H. Watanabe, K. M. C. Fu, K. M. Itoh, and E. Abe, "Dynamic nuclear polarization enhanced magnetic field sensitivity and decoherence spectroscopy of an ensemble of near-surface nitrogen-vacancy centers in diamond," Appl. Phys. Lett. **110**, 192407 (2017).

89. D. Prananto, D. Kikuchi, K. Hayashi, Y. Kainuma, and T. An, "Imaging of stray magnetic field vectors from a magnetic particle with an ensemble of nitrogen-vacancy centers in diamond," Jpn. J. Appl. Phys. **58**, SIIB20 (2019).

90. P. Appel, E. Neu, M. Ganzhorn, A. Barfuss, M. Batzer, M. Gratz, A. Tschoepe, and P. Maletinsky, "Fabrication of all diamond scanning probes for nanoscale magnetometry," Rev. Sci. Instrum. **87**, 063703 (2016).

91. G. Balasubramanian, P. Neumann, D. Twitchen, M. Markham, R. Kolesov, N. Mizuochi, J. Isoya, J. Achard, J. Beck, J. Tissler, V. Jacques, P. R. Hemmer, F. Jelezko, and J. Wrachtrup, "Ultralong spin coherence time in isotopically engineered diamond," Nat. Mater. **8**, 383–387 (2009).

92. L. M. Pham, D. Le Sage, P. L. Stanwix, T. K. Yeung, D. Glenn, A. Trifonov, P. Cappellaro, P. R. Hemmer, M. D. Lukin, H. Park, A. Yacoby, and R. L. Walsworth, "Magnetic field imaging with nitrogen-vacancy ensembles," New J. Phys. **13**, 045021 (2011).

93. P. L. Stanwix, L. M. Pham, J. R. Maze, D. Le Sage, T. K. Yeung, P. Cappellaro, P. R. Hemmer, A. Yacoby, M. D. Lukin, and R. L. Walsworth, "Coherence of nitrogen-vacancy electronic spin ensembles in diamond," Phys. Rev. B **82**, 201201 (2010).

94. T. Ishikawa, K. M. C. Fu, C. Santori, V. M. Acosta, R. G. Beausoleil, H. Watanabe, S. Shikata, and K. M. Itoh, "Optical and spin coherence properties of nitrogen-vacancy centers placed in a 100 nm thick

isotopically purified diamond layer," Nano Lett. **12**, 2083–2087 (2012).

95. A. Jarmola, V. M. Acosta, K. Jensen, S. Chemerisov, and D. Budker, "Temperature- and magnetic-field-dependent longitudinal spin relaxation in nitrogen-vacancy ensembles in diamond," Phys. Rev. Lett. **108**, 197601 (2012).

96. N. Bar-Gill, L. M. Pham, A. Jarmola, D. Budker, and R. L. Walsworth, "Solid-state electronic spin coherence time approaching one second," Nat. Commun. **4**, 1743 (2013).

97. K. Chang, A. Eichler, J. Rhensius, L. Lorenzelli, and C. L. Degen, "Nanoscale imaging of current density with a single-spin magnetometer," Nano Lett. **17**, 2367–2373 (2017).

98. D. Wildanger, B. R. Patton, H. Schill, L. Marseglia, J. P. Hadden, S. Knauer, A. Schoenle, J. G. Rarity, J. L. O'Brien, S. W. Hell, and J. M. Smith, "Solid immersion facilitates fluorescence microscopy with nanometer resolution and sub-angstrom emitter localization," Adv. Mater. **24**, OP309–OP313 (2012).

99. D. Wildanger, J. R. Maze, and S. W. Hell, "Diffraction unlimited all-optical recording of electron spin resonances," Phys. Rev. Lett. **107**, 017601 (2011).

100. S. Arroyo-Camejo, M.-P. Adam, M. Besbes, J.-P. Hugonin, V. Jacques, J.-J. Greffet, J.-F. Roch, S. W. Hell, and F. Treussart, "Stimulated emission depletion microscopy resolves individual nitrogen vacancy centers in diamond nanocrystals," ACS Nano **7**, 10912–10919 (2013).

101. E. Rittweger, K. Y. Han, S. E. Irvine, C. Eggeling, and S. W. Hell, "STED microscopy reveals crystal colour centres with nanometric resolution," Nat. Photonics **3**, 144–147 (2009).

102. E. Rittweger, D. Wildanger, and S. W. Hell, "Far-field fluorescence nanoscopy of diamond color centers by ground state depletion," Europhys. Lett. **86**, 14001 (2009).

103. P. C. Maurer, J. R. Maze, P. L. Stanwix, L. Jiang, A. V. Gorshkov, A. A. Zibrov, B. Harke, J. S. Hodges, A. S. Zibrov, A. Yacoby, D. Twitchen, S. W. Hell, R. L. Walsworth, and M. D. Lukin, "Far-field optical imaging and manipulation of individual spins with nanoscale resolution," Nat. Phys. **6**, 912–918 (2010).

104. J. C. Jaskula, E. Bauch, S. Arroyo-Camejo, M. D. Lukin, S. W. Hell, A. S. Trifonov, and R. L. Walsworth, "Superresolution optical magnetic imaging and spectroscopy using individual electronic spins in diamond," Opt. Express **25**, 11048–11064 (2017).

105. K. Y. Han, S. K. Kim, C. Eggeling, and S. W. Hell, "Metastable dark states enable ground state depletion microscopy of nitrogen vacancy centers in diamond with diffraction-unlimited resolution," Nano Lett. **10**, 3199–3203 (2010).

106. X. Chen, C. Zou, Z. Gong, C. Dong, G. Guo, and F. Sun, "Subdiffraction optical manipulation of the charge state of nitrogen vacancy center in diamond," Light Sci. Appl. **4**, e230 (2015).

107. M. Pfender, N. Aslam, G. Waldherr, P. Neumann, and J. Wrachtrup, "Single-spin stochastic optical reconstruction microscopy," Proc. Natl. Acad. Sci. USA **111**, 14669–14674 (2014).

108. M. Gu, Y. Y. Cao, S. Castelletto, B. Kouskousis, and X. P. Li, "Super-resolving single nitrogen vacancy centers within single nanodiamonds using a localization microscope," Opt. Express **21**, 17639–17646 (2013).

109. F. Bi, M. C. Huang, S. Ryu, H. Lee, C. W. Bark, C. B. Eom, P. Irvin, and J. Levy, "Room-temperature electronically-controlled ferromagnetism at the LaAlO₃/SrTiO₃ interface," Nat. Commun. **5**, 5019 (2014).

110. M. Serri, M. Mannini, L. Poggini, E. Velez-Fort, B. Cortigiani, P. Sainctavit, D. Rovai, A. Caneschi, and R. Sessoli, "Low-temperature magnetic force microscopy on single molecule magnet-based microarrays," Nano Lett. **17**, 1899–1905 (2017).

111. A. Schlenhoff, S. Kovarik, S. Krause, and R. Wiesendanger, "Vacuum resonance states as atomic-scale probes of noncollinear surface magnetism," Phys. Rev. Lett. **123**, 087202 (2019).

112. M. Bode, M. Heide, K. von Bergmann, P. Ferriani, S. Heinze, G. Bihlmayer, A. Kubetzka, O. Pietzsch, S. Blugel, and R. Wiesendanger, "Chiral magnetic order at surfaces driven by inversion asymmetry," Nature **447**, 190–193 (2007).

113. G. Avvisati, C. Cardoso, D. Varsano, A. Ferretti, P. Gargian, and M. G. Betti, "Ferromagnetic and antiferromagnetic coupling of spin

114. N. Bergeard, V. Lopez-Flores, V. Halte, M. Hehn, C. Stamm, N. Pontius, E. Beaurepaire, and C. Boeglin, "Ultrafast angular momentum transfer in multisublattice ferrimagnets," Nat. Commun. **5**, 3466 (2014).

115. T. Ono, H. Miyajima, K. Shigeto, K. Mibu, N. Hosoito, and T. Shinjo, "Propagation of a magnetic domain wall in a submicrometer magnetic wire," Science **284**, 468–470 (1999).

116. M. Tsoi, R. E. Fontana, and S. S. P. Parkin, "Magnetic domain wall motion triggered by an electric current," Appl. Phys. Lett. **83**, 2617–2619 (2003).

117. D. Atkinson, D. A. Allwood, G. Xiong, M. D. Cooke, C. C. Faulkner, and R. P. Cowburn, "Magnetic domain-wall dynamics in a submicrometre ferromagnetic structure," Nat. Mater. **2**, 85–87 (2003).

118. N. Vernier, D. A. Allwood, D. Atkinson, M. D. Cooke, and R. P. Cowbu, "Domain wall propagation in magnetic nanowires by spin-polarized current injection," Europhys. Lett. **65**, 526–532 (2004).

119. A. Yamaguchi, T. Ono, S. Nasu, K. Miyake, K. Mibu, and T. Shinjo, "Real-space observation of current-driven domain wall motion in submicron magnetic wires," Phys. Rev. Lett. **92**, 077205 (2004).

120. I. M. Miron, T. Moore, H. Szambolics, L. D. Buda-Prejbeanu, S. Auffret, B. Rodmacq, S. Pizzini, J. Vogel, M. Bonfim, A. Schuhl, and G. Gaudin, "Fast current-induced domain-wall motion controlled by the Rashba effect," Nat. Mater. **10**, 419–423 (2011).

121. K. S. Ryu, L. Thomas, S. H. Yang, and S. Parkin, "Chiral spin torque at magnetic domain walls," Nat. Nanotechnol. **8**, 527–533 (2013).

122. D. A. Allwood, G. Xiong, C. C. Faulkner, D. Atkinson, D. Petit, and R. P. Cowburn, "Magnetic domain-wall logic," Science **309**, 1688–1692 (2005).

123. S. S. P. Parkin, M. Hayashi, and L. Thomas, "Magnetic domain-wall racetrack memory," Science **320**, 190–194 (2008).

124. M. Hayashi, L. Thomas, R. Moriya, C. Rettner, and S. S. P. Parkin, "Current-controlled magnetic domain-wall nanowire shift register," Science **320**, 209–211 (2008).

125. Z. C. Luo, A. Hrabec, T. P. Dao, G. Sala, S. Finizio, J. X. Feng, S. Mayr, J. Raabe, P. Gambardella, and L. J. Heyderman, "Current-driven magnetic domain-wall logic," Nature **579**, 214–218 (2020).

126. G. S. D. Beach, M. Tsoi, and J. L. Erskine, "Current-induced domain wall motion," J. Magn. Magn. Mater. **320**, 1272–1281 (2008).

127. A. V. Khvalkovskiy, V. Cros, D. Apalkov, V. Nikitin, M. Krounbi, K. A. Zvezdin, A. Anane, J. Grollier, and A. Fert, "Matching domain-wall configuration and spin-orbit torques for efficient domain-wall motion," Phys. Rev. B **87**, 020402 (2013).

128. J. P. Tetienne, T. Hingant, L. Rondin, S. Rohart, A. Thiaville, E. Jue, G. Gaudin, J. F. Roch, and V. Jacques, "Nitrogen-vacancy-center imaging of bubble domains in a 6-angstrom film of cobalt with perpendicular magnetization," J. Appl. Phys. **115**, 17D501 (2014).

129. T. Miyazaki and H. Jin, *The Physics of Ferromagnetism* (Springer Berlin Heidelberg, 2012).

130. J. P. Tetienne, T. Hingant, J. V. Kim, L. H. Diez, J. P. Adam, K. Garcia, J. F. Roch, S. Rohart, A. Thiaville, D. Ravelosona, and V. Jacques, "Nanoscale imaging and control of domain-wall hopping with a nitrogen-vacancy center microscope," Science **344**, 1366–1369 (2014).

131. U. K. Rossler, A. N. Bogdanov, and C. Pfleiderer, "Spontaneous skyrmion ground states in magnetic metals," Nature **442**, 797–801 (2006).

132. S. Muhlbauer, B. Binz, F. Jonietz, C. Pfleiderer, A. Rosch, A. Neubauer, R. Georgii, and P. Boni, "Skyrmion lattice in a chiral magnet," Science **323**, 915–919 (2009).

133. N. Nagaosa and Y. Tokura, "Topological properties and dynamics of magnetic skyrmions," Nat. Nanotechnol. **8**, 899–911 (2013).

134. S. Woo, K. Litzius, B. Kruger, M. Y. Im, L. Caretta, K. Richter, M. Mann, A. Krone, R. M. Reeve, M. Weigand, P. Agrawal, I. Lemesh, M. A. Mawass, P. Fischer, M. Klaui, and G. R. S. D. Beach, "Observation of room-temperature magnetic skyrmions and their current-driven dynamics in ultrathin metallic ferromagnets," Nat. Mater. **15**, 501–506 (2016).

135. X. C. Zhang, Y. Zhou, M. Ezawa, G. P. Zhao, and W. S. Zhao, "Magnetic skyrmion transistor: skyrmion motion in a voltage-gated nanotrack," Sci. Rep. **5**, 11369 (2015).

136. X. C. Zhang, M. Ezawa, and Y. Zhou, "Magnetic skyrmion logic gates: conversion, duplication and merging of skyrmions," Sci. Rep. **5**, 9400 (2015).
137. I. Gross, W. Akhtar, A. Hrabec, J. Sampaio, L. J. Martinez, S. Chouaieb, B. J. Shields, P. Maletinsky, A. Thiaville, S. Rohart, and V. Jacques, "Skyrmion morphology in ultrathin magnetic films," Phys. Rev. Mater. **2**, 024406 (2018).
138. R. J. Blakely, *Potential Theory in Gravity and Magnetic Applications* (Cambridge University, 1996).
139. T. Lenz, G. Chatzidrosos, Z. Wang, L. Bougas, Y. Dumeige, A. Wickenbrock, N. Kerber, J. Zázvorka, F. Kammerbauer, M. Kläui, Z. Kazi, K.-M. C. Fu, K. M. Itoh, H. Watanabe, and D. Budker, "Imaging topological spin structures using light-polarization and magnetic microscopy," Phys. Rev. Appl. **15**, 024040 (2021).
140. T. Kampfrath, A. Sell, G. Klatt, A. Pashkin, S. Mahrlein, T. Dekorsy, M. Wolf, M. Fiebig, A. Leitenstorfer, and R. Huber, "Coherent terahertz control of antiferromagnetic spin waves," Nat. Photonics **5**, 31–34 (2011).
141. R. Khymyn, I. Lisenkov, V. Tiberkevich, B. A. Ivanov, and A. Slavin, "Antiferromagnetic THz-frequency Josephson-like oscillator driven by spin current," Sci. Rep. **7**, 43705 (2017).
142. K. Olejnik, T. Seifert, Z. Kaspar, V. Novak, P. Wadley, R. P. Campion, M. Baumgartner, P. Gambardella, P. Nemec, J. Wunderlich, J. Sinova, P. Kuzel, M. Muller, T. Kampfrath, and T. Jungwirth, "Terahertz electrical writing speed in an antiferromagnetic memory," Sci. Adv. **4**, eaar3566 (2018).
143. T. Jungwirth, X. Marti, P. Wadley, and J. Wunderlich, "Antiferromagnetic spintronics," Nat. Nanotechnol. **11**, 231–241 (2016).
144. L. Smejkal, Y. Mokrousov, B. H. Yan, and A. H. MacDonald, "Topological antiferromagnetic spintronics," Nat. Phys. **14**, 242–251 (2018).
145. P. Appel, B. J. Shields, T. Kosub, N. Hedrich, R. Huebner, J. Fassbender, D. Makarov, and P. Maletinsky, "Nanomagnetism of magnetoelectric granular thin-film antiferromagnets," Nano Lett. **19**, 1682–1687 (2019).
146. L. Thiel, Z. Wang, M. A. Tschudin, D. Rohner, I. Gutierrez-Lezama, N. Ubrig, M. Gibertini, E. Giannini, A. F. Morpurgo, and P. Maletinsky, "Probing magnetism in 2D materials at the nanoscale with single-spin microscopy," Science **364**, 973–976 (2019).
147. A. Agbelele, D. Sando, C. Toulouse, C. Paillard, R. D. Johnson, R. Rüffer, A. F. Popkov, C. Carrétéro, P. Rovillain, J.-M. Le Breton, B. Dkhil, M. Cazayous, Y. Gallais, M.-A. Méasson, A. Sacuto, P. Manuel, A. K. Zvezdin, A. Barthélémy, J. Juraszek, and M. Bibes, "Strain and magnetic field induced spin-structure transitions in multiferroic BiFeO₃," Adv. Mater. **29**, 1602327 (2017).
148. P. Wadley, B. Howells, J. Železný, C. Andrews, V. Hills, R. P. Campion, V. Novák, K. Olejník, F. Maccherozzi, S. S. Dhesi, S. Y. Martin, T. Wagner, J. Wunderlich, F. Freimuth, Y. Mokrousov, J. Kuneš, J. S. Chauhan, M. J. Grzybowski, A. W. Rushforth, K. W. Edmonds, B. L. Gallagher, and T. Jungwirth, "Electrical switching of an antiferromagnet," Science **351**, 587–590 (2016).
149. J. Godinho, H. Reichlova, D. Kriegner, V. Novak, K. Olejnik, Z. Kaspar, Z. Soban, P. Wadley, R. P. Campion, R. M. Otxoa, P. E. Roy, J. Zelezny, T. Jungwirth, and J. Wunderlich, "Electrically induced and detected Néel vector reversal in a collinear antiferromagnet," Nat. Commun. **9**, 4686 (2018).
150. S. Y. Bodnar, L. Smejkal, I. Turek, T. Jungwirth, O. Gomonay, J. Sinova, A. A. Sapozhnik, H. J. Elmers, M. Klaui, and M. Jourdan, "Writing and reading antiferromagnetic Mn₂Au by Néel spin-orbit torques and large anisotropic magnetoresistance," Nat. Commun. **9**, 348 (2018).
151. N. Hedrich, K. Wagner, O. V. Pylypovskyi, B. J. Shields, T. Kosub, D. D. Sheka, D. Makarov, and P. Maletinsky, "Nanoscale mechanics of antiferromagnetic domain walls," Nat. Phys. **17**, 574–577 (2021).
152. U. Schollwöck, J. Richter, D. J. J. Farnell, and R. F. Bishop, *Quantum Magnetism* (Springer Berlin Heidelberg, 2008).
153. A. V. Chumak, V. I. Vasyuchka, A. A. Serga, and B. Hillebrands, "Magnon spintronics," Nat. Phys. **11**, 453–461 (2015).
154. R. Kubo, "Fluctuation-dissipation theorem," Rep. Prog. Phys. **29**, 255 (1966).
155. F. Schwabl, R. Hilton, and A. Lahee, *Advanced Quantum Mechanics* (Springer Berlin Heidelberg, 2008).
156. T. van der Sar, F. Casola, R. Walsworth, and A. Yacoby, "Nanometre-scale probing of spin waves using single-electron spins," Nat. Commun. **6**, 7886 (2015).
157. I. Bertelli, J. J. Carmiggelt, T. Yu, B. G. Simon, C. C. Pothoven, G. E. W. Bauer, Y. M. Blanter, J. Aarts, and T. van der Sar, "Magnetic resonance imaging of spin-wave transport and interference in a magnetic insulator," Sci. Adv. **6**, eabd3556 (2020).
158. D. D. Stancil and A. Prabhakar, *Spin Waves: Theory and Applications* (Springer US, 2009).
159. D. Wesenberg, T. Liu, D. Balzar, M. Z. Wu, and B. L. Zink, "Long-distance spin transport in a disordered magnetic insulator," Nat. Phys. **13**, 987–993 (2017).
160. R. Lebrun, A. Ross, S. A. Bender, A. Qaiumzadeh, L. Baldrati, J. Cramer, A. Brataas, R. A. Duine, and M. Klaui, "Tunable long-distance spin transport in a crystalline antiferromagnetic iron oxide," Nature **561**, 222–225 (2018).
161. K. Vogt, F. Y. Fradin, J. E. Pearson, T. Sebastian, S. D. Bader, B. Hillebrands, A. Hoffmann, and H. Schultheiss, "Realization of a spin-wave multiplexer," Nat. Commun. **5**, 3727 (2014).
162. A. V. Chumak, A. A. Serga, and B. Hillebrands, "Magnon transistor for all-magnon data processing," Nat. Commun. **5**, 4700 (2014).
163. L. J. Cornelissen, J. Liu, B. J. van Wees, and R. A. Duine, "Spin-current-controlled modulation of the magnon spin conductance in a three-terminal magnon transistor," Phys. Rev. Lett. **120**, 097702 (2018).
164. T. Warwick, K. Franck, J. Kortright, G. Meigs, M. Moronne, S. Myneni, E. Rotenberg, S. Seal, W. Steele, and H. Ade, "A scanning transmission X-ray microscope for materials science spectromicroscopy at the advanced light source," Rev. Sci. Instrum. **69**, 2964–2973 (1998).
165. V. Sluka, T. Schneider, R. A. Gallardo, A. Kákay, M. Weigand, T. Warnatz, R. Mattheis, A. Roldán-Molina, P. Landeros, and V. Tiberkevich, "Emission and propagation of 1D and 2D spin waves with nanoscale wavelengths in anisotropic spin textures," Nat. Nanotechnol. **14**, 328–333 (2019).
166. T. Sebastian, K. Schultheiss, B. Obry, B. Hillebrands, and H. Schultheiss, "Micro-focused Brillouin light scattering: imaging spin waves at the nanoscale," Front. Phys. **3**, 35 (2015).
167. Y. Acremann, C. H. Back, M. Buess, O. Portmann, A. Vaterlaus, D. Pescia, and H. Melchior, "Imaging precessional motion of the magnetization vector," Science **290**, 492–495 (2000).
168. C. Du, T. van der Sar, T. X. Zhou, P. Upadhyaya, F. Casola, H. Zhang, M. C. Onbasli, C. A. Ross, R. L. Walsworth, Y. Tserkovnyak, and A. Yacoby, "Control and local measurement of the spin chemical potential in a magnetic insulator," Science **357**, 195–198 (2017).
169. T. Giamarchi, C. Ruegg, and O. Tchernyshyov, "Bose–Einstein condensation in magnetic insulators," Nat. Phys. **4**, 198–204 (2008).
170. B. Flebus and Y. Tserkovnyak, "Quantum-impurity relaxometry of magnetization dynamics," Phys. Rev. Lett. **121**, 187204 (2018).
171. B. Flebus, "Chemical potential of an antiferromagnetic magnon gas," Phys. Rev. B **100**, 064410 (2019).
172. Y. Tserkovnyak, J. Zou, S. K. Kim, and S. Takei, "Quantum hydrodynamics of spin winding," Phys. Rev. B **102**, 224433 (2020).
173. E. Lee-Wong, R. L. Xue, F. Y. Ye, A. Kreisel, T. van Der Sar, A. Yacoby, and C. R. Du, "Nanoscale detection of magnon excitations with variable wavevectors through a quantum spin sensor," Nano Lett. **20**, 3284–3290 (2020).
174. A. Rustagi, I. Bertelli, T. van der Sar, and P. Upadhyaya, "Sensing chiral magnetic noise via quantum impurity relaxometry," Phys. Rev. B **102**, 220403 (2020).
175. K. R. Joshi, N. M. Nusran, M. A. Tanatar, K. Cho, W. R. Meier, S. L. Bud'ko, P. C. Canfield, and R. Prozorov, "Measuring the lower critical field of superconductors using nitrogen-vacancy centers in diamond optical magnetometry," Phys. Rev. Appl. **11**, 014035 (2019).

176. S. Hsieh, P. Bhattacharyya, C. Zu, T. Mittiga, T. J. Smart, F. Machado, B. Kobrin, T. O. Hoehn, N. Z. Rui, M. Kamrani, S. Chatterjee, S. Choi, M. Zaletel, V. V. Struzhkin, J. E. Moore, V. I. Levitas, R. Jeanloz, and N. Y. Yao, "Imaging stress and magnetism at high pressures using a nanoscale quantum sensor," Science **366**, 1349–1354 (2019).

177. V. M. Acosta, L. S. Bouchard, D. Budker, R. Folman, T. Lenz, P. Maletinsky, D. Rohner, Y. Schlussel, and L. Thiel, "Color centers in diamond as novel probes of superconductivity," J. Supercond. Novel Magn. **32**, 85–95 (2019).

178. A. Waxman, Y. Schlussel, D. Groswasser, V. M. Acosta, L. S. Bouchard, D. Budker, and R. Folman, "Diamond magnetometry of superconducting thin films," Phys. Rev. B **89**, 054509 (2014).

179. N. Alfasi, S. Masis, O. Shtempluck, V. Kochetok, and E. Buks, "Diamond magnetometry of Meissner currents in a superconducting film," AIP Adv. **6**, 075311 (2016).

180. Y. Schlussel, T. Lenz, D. Rohner, Y. Bar-Haim, L. Bougas, D. Groswasser, M. Kieschnick, E. Rozenberg, L. Thiel, A. Waxman, J. Meijer, P. Maletinsky, D. Budker, and R. Folman, "Wide-field imaging of superconductor vortices with electron spins in diamond," Phys. Rev. Appl. **10**, 034032 (2018).

181. C. Buzea and T. Yamashita, "Review of the superconducting properties of MgB$_2$," Supercond. Sci. Technol. **14**, R115 (2001).

182. A. P. Drozdov, M. I. Eremets, I. A. Troyan, V. Ksenofontov, and S. I. Shylin, "Conventional superconductivity at 203 kelvin at high pressures in the sulfur hydride system," Nature **525**, 73–76 (2015).

183. M. Somayazulu, M. Ahart, A. K. Mishra, Z. M. Geballe, M. Baldini, Y. Meng, V. V. Struzhkin, and R. J. Hemley, "Evidence for superconductivity above 260 K in lanthanum superhydride at megabar pressures," Phys. Rev. Lett. **122**, 027001 (2019).

184. A. P. Drozdov, P. P. Kong, V. S. Minkov, S. P. Besedin, M. A. Kuzovnikov, S. Mozaffari, L. Balicas, F. F. Balakirev, D. E. Graf, V. B. Prakapenka, E. Greenberg, D. A. Knyazev, M. Tkacz, and M. I. Eremets, "Superconductivity at 250 K in lanthanum hydride under high pressures," Nature **569**, 528–531 (2019).

185. I. A. Kruglov, A. G. Kvashnin, A. F. Goncharov, A. R. Oganov, S. S. Lobanov, N. Holtgrewe, S. Jiang, V. B. Prakapenka, E. Greenberg, and A. V. Yanilkin, "Uranium polyhydrides at moderate pressures: prediction, synthesis, and expected superconductivity," Sci. Adv. **4**, eaat9776 (2018).

186. E. Snider, N. Dasenbrock-Gammon, R. McBride, M. Debessai, H. Vindana, K. Vencatasamy, K. V. Lawler, A. Salamat, and R. P. Dias, "Room-temperature superconductivity in a carbonaceous sulfur hydride," Nature **586**, 373–377 (2020).

187. D. Rohner, L. Thiel, B. Muller, M. Kasperczyk, R. Kleiner, D. Koelle, and P. Maletinsky, "Real-space probing of the local magnetic response of thin-film superconductors using single spin magnetometry," Sensors **18**, 3790 (2018).

188. M. Tinkham, *Introduction to Superconductivity* (Courier Corporation, 2004).

189. C. R. Hu, "Numerical constants for isolated vortices in superconductors," Phys. Rev. B **6**, 1756–1760 (1972).

190. C. P. Bean and J. D. Livingston, "Surface barrier in Type-2 superconductors," Phys. Rev. Lett. **12**, 14–16 (1964).

191. E. H. Brandt, "The flux-line-lattice in superconductors," Rep. Prog. Phys. **58**, 1465–1594 (1995).

192. E. H. Brandt, "Geometric barrier and current string in type-II superconductors obtained from continuum electrodynamics," Phys. Rev. B **59**, 3369–3372 (1999).

193. J. Pearl, "Current distribution in superconducting films carrying quantized fluxoids," Appl. Phys. Lett. **5**, 65–66 (1964).

194. G. Carneiro and E. H. Brandt, "Vortex lines in films: fields and interactions," Phys. Rev. B **61**, 6370–6376 (2000).

195. B. Weber, S. Mahapatra, H. Ryu, S. Lee, A. Fuhrer, T. C. G. Reusch, D. L. Thompson, W. C. T. Lee, G. Klimeck, L. C. L. Hollenberg, and M. Y. Simmons, "Ohm's law survives to the atomic scale," Science **335**, 64–67 (2012).

196. B. G. Park, S. W. Hwang, and Y. J. Park, *Nanoelectronic Devices* (Jenny Stanford Publishing, 2012).

197. Y. Liu, N. O. Weiss, X. D. Duan, H. C. Cheng, Y. Huang, and X. F. Duan, "Van der Waals heterostructures and devices," Nat. Rev. Mater. **1**, 16042 (2016).

198. Y. Liu, X. D. Duan, H. J. Shin, S. Park, Y. Huang, and X. F. Duan, "Promises and prospects of two-dimensional transistors," Nature **591**, 43–53 (2021).

199. J. H. Chen, C. Jang, S. Adam, M. S. Fuhrer, E. D. Williams, and M. Ishigami, "Charged-impurity scattering in graphene," Nat. Phys. **4**, 377–381 (2008).

200. A. W. Tsen, L. Brown, M. P. Levendorf, F. Ghahari, P. Y. Huang, R. W. Havener, C. S. Ruiz-Vargas, D. A. Muller, P. Kim, and J. Park, "Tailoring electrical transport across grain boundaries in polycrystalline graphene," Science **336**, 1143–1146 (2012).

201. D. Collomb, P. L. Li, and S. J. Bending, "Nanoscale graphene Hall sensors for high-resolution ambient magnetic imaging," Sci. Rep. **9**, 14424 (2019).

202. F. S. Wells, A. V. Pan, I. A. Golovchanskiy, S. A. Fedoseev, and A. Rozenfeld, "Observation of transient overcritical currents in YBCO thin films using high-speed magneto-optical imaging and dynamic current mapping," Sci. Rep. **7**, 40235 (2017).

203. D. Vasyukov, Y. Anahory, L. Embon, D. Halbertal, J. Cuppens, L. Neeman, A. Finkler, Y. Segev, Y. Myasoedov, M. L. Rappaport, M. E. Huber, and E. Zeldov, "A scanning superconducting quantum interference device with single electron spin sensitivity," Nat. Nanotechnol. **8**, 639–644 (2013).

204. J.-P. Tetienne, N. Dontschuk, D. A. Broadway, A. Stacey, D. A. Simpson, and L. C. L. Hollenberg, "Quantum imaging of current flow in graphene," Sci. Adv. **3**, e1602429 (2017).

205. S. E. Lillie, N. Dontschuk, D. A. Broadway, D. L. Creedon, L. C. L. Hollenberg, and J.-P. Tetienne, "Imaging graphene field-effect transistors on diamond using nitrogen-vacancy microscopy," Phys. Rev. Appl. **12**, 024018 (2019).

206. B. B. Zhou, P. C. Jerger, K.-H. Lee, M. Fukami, F. Mujid, J. Park, and D. D. Awschalom, "Spatiotemporal mapping of a photocurrent vortex in Monolayer MoS2 using diamond quantum sensors," Phys. Rev. X **10**, 011003 (2020).

207. M. J. H. Ku, T. X. Zhou, Q. Li, Y. J. Shin, J. K. Shi, C. Burch, L. E. Anderson, A. T. Pierce, Y. Xie, A. Hamo, U. Vool, H. Zhang, F. Casola, T. Taniguchi, K. Watanabe, M. M. Fogler, P. Kim, A. Yacoby, and R. L. Walsworth, "Imaging viscous flow of the Dirac fluid in graphene," Nature **583**, 537–541 (2020).

208. T. I. Andersen, B. L. Dwyer, J. D. Sanchez-Yamagishi, J. F. Rodriguez-Nieva, K. Agarwal, K. Watanabe, T. Taniguchi, E. A. Demler, P. Kim, H. Park, and M. D. Lukin, "Electron-phonon instability in graphene revealed by global and local noise probes," Science **364**, 154–157 (2019).

209. L. Jiang, J. S. Hodges, J. R. Maze, P. Maurer, J. M. Taylor, D. G. Cory, P. R. Hemmer, R. L. Walsworth, A. Yacoby, A. S. Zibrov, and M. D. Lukin, "Repetitive readout of a single electronic spin via quantum logic with nuclear spin ancillae," Science **326**, 267–272 (2009).

210. G. Waldherr, J. Beck, P. Neumann, R. S. Said, M. Nitsche, M. L. Markham, D. J. Twitchen, J. Twamley, F. Jelezko, and J. Wrachtrup, "High-dynamic-range magnetometry with a single nuclear spin in diamond," Nat. Nanotechnol. **7**, 105–108 (2012).

211. C. Bonato, M. S. Blok, H. T. Dinani, D. W. Berry, M. L. Markham, D. J. Twitchen, and R. Hanson, "Optimized quantum sensing with a single electron spin using real-time adaptive measurements," Nat. Nanotechnol. **11**, 247–252 (2016).

212. S. Kolkowitz, A. Safira, A. A. High, R. C. Devlin, S. Choi, Q. P. Unterreithmeier, D. Patterson, A. S. Zibrov, V. E. Manucharyan, H. Park, and M. D. Lukin, "Probing Johnson noise and ballistic transport in normal metals with a single-spin qubit," Science **347**, 1129–1132 (2015).

213. L. S. Langsjoen, A. Poudel, M. G. Vavilov, and R. Joynt, "Qubit relaxation from evanescent-wave Johnson noise," Phys. Rev. A **86**, 010301 (2012).

214. H. N. Spector, "Amplification of acoustic waves through interaction with conduction electrons," Phys. Rev. **127**, 1084–1090 (1962).

215. A. B. Pippard, "Acoustic amplification in semiconductors and metals," Philos. Mag. **8**, 161–165 (1963).

216. S. M. Komirenko, K. W. Kim, A. A. Demidenko, V. A. Kochelap, and M. A. Stroscio, "Generation and amplification of sub-THz coherent acoustic phonons under the drift of two-dimensional electrons," Phys. Rev. B **62**, 7459–7469 (2000).

217. C. X. Zhao, W. Xu, and F. M. Peeters, "Cerenkov emission of terahertz acoustic-phonons from graphene," Appl. Phys. Lett. **102**, 222101 (2013).

218. J. M. Boss, K. Cujia, J. Zopes, and C. L. Degen, "Quantum sensing with arbitrary frequency resolution," Science **356**, 837–840 (2017).

219. S. Schmitt, T. Gefen, F. M. Stürner, T. Unden, G. Wolff, C. Müller, J. Scheuer, B. Naydenov, M. Markham, and S. Pezzagna, "Submillihertz magnetic spectroscopy performed with a nanoscale quantum sensor," Science **356**, 832–837 (2017).

220. R. K. Pathria and P. D. Beale, *Statistical Mechanics* (Elsevier, 2011).

221. C. L. Degen, F. Reinhard, and P. Cappellaro, "Quantum sensing," Rev. Mod. Phys. **89**, 035002 (2017).

222. L. Levitov and G. Falkovich, "Electron viscosity, current vortices and negative nonlocal resistance in graphene," Nat. Phys. **12**, 672–676 (2016).

223. M. Chandra, G. Kataria, D. Sahdev, and R. Sundararaman, "Hydrodynamic and ballistic AC transport in two-dimensional Fermi liquids," Phys. Rev. B **99**, 165409 (2019).

224. B. Flebus, H. Ochoa, P. Upadhyaya, and Y. Tserkovnyak, "Proposal for dynamic imaging of antiferromagnetic domain wall via quantum-impurity relaxometry," Phys. Rev. B **98**, 180409 (2018).

225. S. Chatterjee, P. E. Dolgirev, I. Esterlis, A. A. Zibrov, M. D. Lukin, N. Y. Yao, and E. Demler, "Single-spin qubit magnetic spectroscopy of two-dimensional superconductivity," Phys. Rev. Res. **4**, L012001 (2022).

226. J. F. Rodriguez-Nieva, K. Agarwal, T. Giamarchi, B. I. Halperin, M. D. Lukin, and E. Demler, "Probing one-dimensional systems via noise magnetometry with single spin qubits," Phys. Rev. B **98**, 195433 (2018).

227. Q.-D. Jiang and F. Wilczek, "Quantum atmospherics for materials diagnosis," Phys. Rev. B **99**, 201104 (2019).